AD-A183 955 A SIXTEEN NODE SHELL ELEMENT WITH A MATRIX STABILIZATION SCHEME(U) MARYLAND UNIV COLLEGE PARK DEPT OF AEROSPACE ENGINEERING J J RHIU ET AL. 22 APR 87 1/1

UNCLASSIFIED N00014-84-K-0305 F/G 20/11 NL

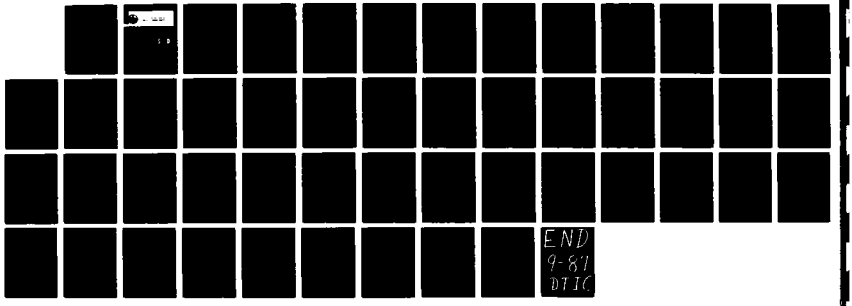

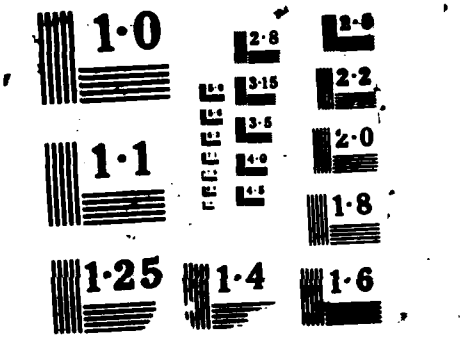
1·0
1·1
1·25
2·8
3·15
3·5
4·0
1·4
2·2
2·0
1·8
1·6

University of Maryland, College Park
Department of Aerospace Engineering

A SIXTEEN NODE SHELL ELEMENT WITH A MATRIX STABILIZATION SCHEME

J.J. RHIU

S.W. LEE

April 1987

INTERIM REPORT

Office of Naval Research
Contract No. N00014-84-K-0385
Work Unit No. 4324-718

SECURITY CLASSIFICATION OF THIS PAGE

REPORT DOCUMENTATION PAGE

1a. REPORT SECURITY CLASSIFICATION: Unclassified	1b. RESTRICTIVE MARKINGS:
2a. SECURITY CLASSIFICATION AUTHORITY:	3. DISTRIBUTION/AVAILABILITY OF REPORT: Unlimited
2b. DECLASSIFICATION/DOWNGRADING SCHEDULE:	
4. PERFORMING ORGANIZATION REPORT NUMBER(S):	5. MONITORING ORGANIZATION REPORT NUMBER(S):
6a. NAME OF PERFORMING ORGANIZATION: Department of Aerospace Eng. University of Maryland; 6b. OFFICE SYMBOL (If applicable):	7a. NAME OF MONITORING ORGANIZATION: Office of Naval Research Mechanics Division
6c. ADDRESS (City, State and ZIP Code): College Park, Maryland 20742	7b. ADDRESS (City, State and ZIP Code): 800 North Quincy Street Arlington, VA 22217
8a. NAME OF FUNDING/SPONSORING ORGANIZATION: Office of Naval Research; 8b. OFFICE SYMBOL (If applicable):	9. PROCUREMENT INSTRUMENT IDENTIFICATION NUMBER: N00014-84-K-0385
8c. ADDRESS (City, State and ZIP Code): 800 North Quincy Street Arlington, VA 22217	10. SOURCE OF FUNDING NOS. — PROGRAM ELEMENT NO.: ; PROJECT NO.: ; TASK NO.: ; WORK UNIT NO.: 4324-718
11. TITLE (Include Security Classification): A Sixteen Node Shell Element with a Matrix Stabilization Scheme	
12. PERSONAL AUTHOR(S): J.J. Rhiu and S.W. Lee	
13a. TYPE OF REPORT: Interim; 13b. TIME COVERED FROM Oct. 1986 TO Mar 1987	14. DATE OF REPORT (Yr., Mo., Day): April 22, 1987; 15. PAGE COUNT: 47
16. SUPPLEMENTARY NOTATION:	

17. COSATI CODES			18. SUBJECT TERMS (Continue on reverse if necessary and identify by block number)
FIELD	GROUP	SUB. GR.	Sixteen-Node shell element, Hellinger-Reissner principle assumed strain, kinematic mdoes, locking

19. ABSTRACT (Continue on reverse if necessary and identify by block number)

A sixteen node shell element is developed using a matrix stabilization scheme based on the Hellinger-Reissner principle with independent strain. Initially the assumed independent strain is divided into a lower order part and a higher order part. The stiffness matrix corresponding to the lower order assumed strain is equivalent to the stiffness matrix of the assumed displacement model element with the reduced integration scheme. The spurious kinematic modes of the element are supporessed by introducing a stabilization matrix associated with a judiciously chosen set of higher order assumed strain fields. Numerical resutls show that this element is free of locking even for very thin plates and shells.

20. DISTRIBUTION/AVAILABILITY OF ABSTRACT: UNCLASSIFIED/UNLIMITED ☑ SAME AS RPT. ☐ OTIC USERS ☐	21. ABSTRACT SECURITY CLASSIFICATION: Unclassified
22a. NAME OF RESPONSIBLE INDIVIDUAL: Dr. R.E. Whitehead, Mechanics Division, ONR	22b. TELEPHONE NUMBER (Include Area Code): 202-696-4305; 22c. OFFICE SYMBOL:

DD FORM 1473, 83 APR EDITION OF 1 JAN 73 IS OBSOLETE.

Unclassified
SECURITY CLASSIFICATION OF THIS PAGE

A SIXTEEN NODE SHELL ELEMENT

WITH A MATRIX STABILIZATION SCHEME

J.J. RHIU

S.W. LEE

April 1987

INTERIM REPORT

Office of Naval Research
Contract No. N00014-84-K-0385
Work Unit No. 4324-718

ABSTRACT

A sixteen node shell element is developed using a matrix stabilization scheme based on the Hellinger-Reissner principle with independent strain. Initially the assumed independent strain is divided into a lower order part and a higher order part. The stiffness matrix corresponding to the lower order assumed strain is equivalent to the stiffness matrix of the assumed displacement model element with the reduced integration scheme. The spurious kinematic modes of the element are suppressed by introducing a stabilization matrix associated with a judiciously chosen set of higher order assumed strain fields. Numerical results show that this element is free of locking even for very thin plates and shells.

INTRODUCTION

Since the early days in the history of the finite element method, a great deal of research effort has been directed to the finite element modeling of thin shell structures. Among all existing approaches, the degenerate solid shell element concept [Ahmad, Irons and Zienkiewicz (1970)] appears to be the most convenient for the description of the arbitrary shell geometry and the kinematics of deformation. However, it is well known that the degenerate solid shell elements exhibit a serious drawback unless special care is taken. This phenomenon, known as locking, arises from the overstiffening effect due to the conditions of zero inplane strain and zero transverse shear strain when the shell thickness becomes small [Lee and Pian (1978)].

A very popular way of alleviating locking has been to utilize the reduced or selective integration scheme [Zienkiewicz, Too and Taylor (1971); Pawsey and Clough (1971); Hughes, Cohen and Haroun (1978); Pugh, Hinton and Zienkiewicz (1978); Stolarski and Belytschko (1982)]. However, the reduced or selective integration scheme has not been successful in eliminating the effect of locking

completely. Even with the 2x2x2 point reduced integration, an eight node shell element based on the assumed displacement finite element model still experiences locking. On the other hand, the 2x2x2 point reduced integration rule applied to a nine node element or the 3x3x2 point reduced integration rule applied to a sixteen node element eliminates the effect of locking. However, they introduce spurious kinematic modes which lead to unstable finite element models. To improve the kinematic stability, we may employ selective integration schemes to these elements in which a higher order integration rule is used for the bending part. However, selective integration schemes cannot eliminate the unstable spurious kinematic modes completely. In short, it is not easy to find an appropriate reduced or selective integration rule which can eliminate both locking and undesirable kinematic modes at the same time.

In order to suppress the spurious kinematic modes, we may add a stabilization matrix to the element stiffness matrix evaluated by a reduced integration rule [Belytschko, Ong and Liu (1984); Belytschko, Liu, Ong and Lam (1985)]. In doing so, great care is needed to avoid reintroducing the effect of locking through excessive stabilization. Recently, a rational method of generating a stabilization matrix has been developed [Lee and Rhiu (1986)]. This method is based on the Hellinger-Reissner principle including both independent strain and displacement-dependent strain. The assumed independent strain is divided into a lower order part and a higher order part. With a proper integration rule, the lower order assumed strain leads to an element stiffness matrix equivalent to that based on the assumed displacement model evaluated with the same integration rule [Lee (1978); Malkus and Hughes (1978)]. A judiciously chosen higher order independent strain field is used to generate a stabilization matrix. Following this approach, a nine node element which is free of locking and undesirabe spurious kinematic modes has been developed for the analysis of thin shell

structures [Rhiu and Lee (1987); Rhiu (1985)].

Encouraged by this success, we extend in this paper the new approach to the formulation of a sixteen node degenerate solid shell element. Since displacement fields are assumed bicubic, the sixteen node element has the potential to represent shell behavior with considerable accuracy. However, with the 4x4x2 point integration, the sixteen node element based on the assumed displacement model still suffers from locking, particularly for distorted or curved finite element meshes. On the other hand, as mentioned previously, the element stiffness matrix evaluated by the 3x3x2 point reduced integration rule has unstable spurious kinematic modes. These spurious kinematic modes will be identified. Then they will be suppressed by adding a stabilization matrix which is derived through the use of appropriately assumed higher order independent strain fields. Finally, the performance of the present element will be tested by solving example problems.

GEOMETRY AND KINEMATICS

Figure 1 shows the midsurface of a curved sixteen node shell element. In order to describe the shell geometry and the kinematics of deformation, local coordinates with components x, y and z are defined on the shell midsurface in addition to global coordinates with components X, Y and Z. The x, y and z axes of the local coordinate system are parallel to the orthogonal unit vectors $\underset{\sim}{a}_1$, $\underset{\sim}{a}_2$ and $\underset{\sim}{a}_3$ respectively. The unit vectors $\underset{\sim}{a}_1$ and $\underset{\sim}{a}_2$ are tangential to the shell midsurface while $\underset{\sim}{a}_3$ is normal to the surface. The $\underset{\sim}{a}_1$, $\underset{\sim}{a}_2$ and $\underset{\sim}{a}_3$ vectors are given at each node as an input. In addition, they are defined at each integration point in a manner which will be discussed later.

With the coordinate systems described above, the global position vector $\underset{\sim}{X}$ of a generic material point can be expressed as

$$\underset{\sim}{X} = \underset{\sim}{X}_0 + \zeta \frac{t}{2} \underset{\sim}{a}_3 \tag{1}$$

where $\underset{\sim}{X}_0$ is the global position vector of a point located on the shell midsurface, $\zeta \frac{t}{2} \underset{\sim}{a}_3$ is a vector drawn from the point on the midsurface to the generic material point, t is the shell thickness and the nondimensional coordinate ζ runs from -1 to 1. Assuming the shell undergoes small deformation, the displacement vector $\underset{\sim}{U}$ of the generic material point with respect to the global coordinate system can be expressed as

$$\underset{\sim}{U} = \underset{\sim}{U}_0 + \zeta \frac{t}{2} \underset{\sim}{b} \underset{\sim}{\theta} \tag{2}$$

where

$$\underset{\sim}{b} = [-\underset{\sim}{a}_2, \underset{\sim}{a}_1] \tag{2a}$$

$$\underset{\sim}{\theta} = \begin{Bmatrix} \theta_1 \\ \theta_2 \end{Bmatrix} \tag{2b}$$

In Eq. (2b), θ_1 and θ_2 represent small rotations of $\underset{\sim}{a}_3$ around the x and y axes respectively. In Eq. (2), the global displacement vector $\underset{\sim}{U}_0$ of the point on the shell midsurface is related to the corresponding local displacement vector $\underset{\sim}{u}$ with components u, v and w through a transformation matrix $\underset{\sim}{T}$ such that

$$\underset{\sim}{U}_0 = \underset{\sim}{T} \underset{\sim}{u} \tag{3a}$$

$$\underset{\sim}{T} = [\underset{\sim}{a}_1, \underset{\sim}{a}_2, \underset{\sim}{a}_3] \tag{3b}$$

Then introducing the isoparametric representation, Eqs. (1) and (2) can be expressed as

$$\underset{\sim}{X} = \sum_{i=1}^{16} N_i(\xi,n) \underset{\sim}{X}_0^i + \frac{1}{2} \zeta \sum_{i=1}^{16} N_i(\xi,n) t_i \underset{\sim}{a}_3^i \tag{4}$$

$$\underset{\sim}{U} = \sum_{i=1}^{16} N_i(\xi,n) \underset{\sim}{T}_i \underset{\sim}{u}_i + \frac{1}{2} \zeta \sum_{i=1}^{16} N_i(\xi,n) t_i \underset{\sim}{b}_i \underset{\sim}{\theta}_i \tag{5}$$

where $\underset{\sim}{X}_0^i$, t_i, $\underset{\sim}{a}_3^i$, $\underset{\sim}{T}_i$, $\underset{\sim}{u}_i$, $\underset{\sim}{b}_i$, $\underset{\sim}{\theta}_i$ are the values of $\underset{\sim}{X}_0$, t, $\underset{\sim}{a}_3$, $\underset{\sim}{T}$, $\underset{\sim}{u}$, $\underset{\sim}{b}$, $\underset{\sim}{\theta}$ at node i, and N_i is the bicubic shape function in parent coordinates ξ and n.

With the description of $\underset{\sim}{X}$ and $\underset{\sim}{U}$ in Eqs. (4) and (5), the displacement-

dependent strain vector defined with respect to the global coordinate system can be expressed in terms of the vector of nodal degrees of freedom. Then, using strain transformation, the strain vector $\underset{\sim}{\bar{E}}$ in the local coordinate system is written symbolically as

$$\begin{aligned} \underset{\sim}{\bar{E}} &= \lfloor \bar{E}_{xx}\ \bar{E}_{yy}\ \bar{E}_{xy}\ \bar{E}_{yz}\ \bar{E}_{zx} \rfloor^T \\ &= \underset{\sim}{B}(\xi,\eta,\zeta)\ \underset{\sim}{q}_e \end{aligned} \tag{6}$$

where $\underset{\sim}{B}(\xi,\eta,\zeta)$ is the strain-displacement transformation matrix and the element nodal degrees of freedom vector $\underset{\sim}{q}_e$ is expressed as:

$$\underset{\sim}{q}_e^T = \lfloor \underset{\sim}{u}_1^T\ \underset{\sim}{\theta}_1^T,\ \underset{\sim}{u}_2^T\ \underset{\sim}{\theta}_2^T,\ \ldots\ldots,\ \underset{\sim}{u}_{16}^T\ \underset{\sim}{\theta}_{16}^T \rfloor \tag{7}$$

FINITE ELEMENT FORMULATION

For the generation of our sixteen node shell element, we utilize the Hellinger-Reissner functional π_R expressed as follows:

$$\pi_R = \int \left(\underset{\sim}{E}^T\ \underset{\sim}{C}\ \underset{\sim}{\bar{E}} - \frac{1}{2}\ \underset{\sim}{E}^T\ \underset{\sim}{C}\ \underset{\sim}{E} \right) dV - W \tag{8}$$

where $\underset{\sim}{\bar{E}}$ is the displacement-dependent local strain vector given in Eq. (6) and $\underset{\sim}{E}$ is the independent local strain vector such that

$$\underset{\sim}{E} = \lfloor E_{xx}\ E_{yy}\ E_{xy}\ E_{yz}\ E_{zx} \rfloor^T \tag{9}$$

In the present formulation, the independent strain components are assumed to be linear at most through shell thickness. In addition, in Eq. (8), W represents the applied load term, V is the volume of shell and $\underset{\sim}{C}$ is a 5x5 elastic coefficient matrix.

Following Lee and Rhiu (1986), initially the independent strain $\underset{\sim}{E}$ is divided into two parts such that

$$\underset{\sim}{\varepsilon} = \underset{\sim}{\varepsilon}_L + \underset{\sim}{\varepsilon}_H \tag{10}$$

where $\underset{\sim}{\varepsilon}_L$ is the independent strain vector with lower order assumed polynomial terms in ξ, η and $\underset{\sim}{\varepsilon}_H$ is the higher order independent strain vector. Substituting this expression into Eq. (8), the functional π_R becomes

$$\pi_R = \sum U_e - W \tag{11}$$

where

$$U_e = \int (\underset{\sim}{\varepsilon}_L^T \underset{\sim}{C} \bar{\underset{\sim}{\varepsilon}} - \frac{1}{2} \underset{\sim}{\varepsilon}_L^T \underset{\sim}{C} \underset{\sim}{\varepsilon}_L) \, dV - \frac{1}{2} \int \underset{\sim}{\varepsilon}_H^T \underset{\sim}{C} \underset{\sim}{\varepsilon}_H \, dV$$

$$+ \int \underset{\sim}{\varepsilon}_H^T \underset{\sim}{C} (\bar{\underset{\sim}{\varepsilon}} - \underset{\sim}{\varepsilon}_L) \, dV \tag{12}$$

and $\sum$ indicates summation or assembly over all elements.

For a sixteen node element of flat rectangular geometry, the displacement-dependent strain $\bar{\underset{\sim}{\varepsilon}}$ is cubic at most in ξ and η. If the lower order independent strain $\underset{\sim}{\varepsilon}_L$ is assumed to be biquadratic in ξ and η, the first integrals in Eq. (12) can be integrated exactly in ξ-η plane by the 3x3 point Gaussian integration rule. The remaining terms are integrated by the 4x4 point rule over ξ and η. Although these integration rules are determined based on the flat rectangular element geometry, the same integration rules will be adopted for elements with arbitrary geometry. In ζ-direction, the two point integration rule is used. In addition, the assumed lower order independent strain can be expressed such that

$$\underset{\sim}{\varepsilon}_L = \sum_{i=1}^{18} \bar{N}_i(\xi,\eta,\zeta) \, \bar{\underset{\sim}{\varepsilon}}_i = \sum_{i=1}^{18} \bar{N}_i(\xi,\eta,\zeta) \, \underset{\sim}{B}(\xi_i,\eta_i,\zeta_i) q_e$$

$$= \bar{\underset{\sim}{B}}(\xi,\eta,\zeta) \, q_e \tag{13}$$

with

$$\bar{\underset{\sim}{B}} = \sum_{i=1}^{18} \bar{N}_i(\xi,\eta,\zeta) \, \underset{\sim}{B}(\xi_i,\eta_i,\zeta_i) \tag{13a}$$

In Eq. (13), shape function $\bar{N}_i$ is biquadratic in ξ, η and linear in ζ such that $\bar{N}_i = 1$ at point i of the 3x3x2 lower order integration points and zero at other

points, and $\overline{\underset{\sim}{E}}_i$ is the value of $\overline{\underset{\sim}{E}}$ at lower order integration point i. Then, for the lower order strains, it is possible to set

$$\underset{\sim}{E}_L = \overline{\underset{\sim}{E}} \tag{14}$$

at the 3x3x2 integration points.

Applying the adopted integration rules and introducing the equivalence given in Eq. (14), U_e in Eq. (12) can be written as

$$U_e = \frac{1}{2} \int_L \underset{\sim}{E}_L^T \underset{\sim}{C} \underset{\sim}{E}_L \, dV - \frac{1}{2} \int_H \underset{\sim}{E}_H^T \underset{\sim}{C} \underset{\sim}{E}_H \, dV$$

$$+ \int_H \underset{\sim}{E}_H^T \underset{\sim}{C} (\overline{\underset{\sim}{E}} - \underset{\sim}{E}_L) \, dV \tag{15}$$

In the above expression, letters L and H under the integral signs represent the lower order integration (3x3x2 points) and the higher order integration (4x4x2 points) rules, respectively.

Based on the limitation principle [Fraejis de Veubeke (1965)], the polynomial terms in the assumed strain $\underset{\sim}{E}_H$ cannot be of higher order than cubic in ξ and η. Then, with biquadratic $\underset{\sim}{E}_L$, the term containing $\underset{\sim}{E}_L$ in the last integral of Eq. (15) can be integrated by the 3x3x2 point integration rule. Noting this, U_e can be rewritten as

$$U_e = \frac{1}{2} \int_L \underset{\sim}{E}_L^T \underset{\sim}{C} \underset{\sim}{E}_L \, dV - \frac{1}{2} \int_H \underset{\sim}{E}_H^T \underset{\sim}{C} \underset{\sim}{E}_H \, dV$$

$$+ \int_H \underset{\sim}{E}_H^T \underset{\sim}{C} \overline{\underset{\sim}{E}} \, dA - \int_L \underset{\sim}{E}_H^T \underset{\sim}{C} \underset{\sim}{E}_L \, dV \tag{16}$$

Rhiu and Lee (1987) developed a nine node shell element using the expression for U_e equivalent to Eq. (16). For the present sixteen node shell element, the expressions in Eq. (15) is used.

On the other hand, the higher order assumed strain is expressed as

$$\underset{\sim}{\varepsilon}_H = \underset{\sim}{P}(\xi,\eta,\zeta)\ \underset{\sim}{\alpha} \tag{18}$$

where $\underset{\sim}{P}$ is the assumed strain shape function matrix which contain higher order terms in ξ, η and $\underset{\sim}{\alpha}$ is the vector of higher order strain parameters. Note that the $\underset{\sim}{P}$ matrix is linear in ζ.

Introducing Eqs. (6), (13) and (18) into Eq. (15), the functional π_R in Eq. (11) becomes

$$\pi_R = \sum \left(\frac{1}{2}\, q_e^T\, \underset{\sim}{K}_L\, q_e + \underset{\sim}{\alpha}^T\, \underset{\sim}{G}\, q_e - \frac{1}{2}\, \underset{\sim}{\alpha}^T\, \underset{\sim}{H}\, \underset{\sim}{\alpha} - q_e^T\, Q_e\right) \tag{19}$$

where

$$\underset{\sim}{K}_L = \int_L \underset{\sim}{\overline{B}}^T\, \underset{\sim}{C}\, \underset{\sim}{\overline{B}}\ dV \tag{20}$$

$$\underset{\sim}{G} = \int_H \underset{\sim}{P}^T\, \underset{\sim}{C}\, (\underset{\sim}{B} - \underset{\sim}{\overline{B}})\ dV \tag{21}$$

$$\underset{\sim}{H} = \int_H \underset{\sim}{P}^T\, \underset{\sim}{C}\, \underset{\sim}{P}\ dV \tag{22}$$

$$\sum q_e^T\, Q_e = W \tag{23}$$

Setting $\delta\pi_R = 0$ with respect to $\underset{\sim}{\alpha}$ results in the compatibility equation in discretized form as follows:

$$\underset{\sim}{\alpha} = \underset{\sim}{H}^{-1}\, \underset{\sim}{G}\ q_e \tag{24}$$

for each element.

By introducing Eq. (24) into Eq. (19), π_R can be written as

$$\pi_R = \sum \left(\frac{1}{2}\, q_e^T\, \underset{\sim}{K}_e\, q_e - q_e^T\, Q_e\right) \tag{25}$$

In the above equation, the element stiffness matrix $\underset{\sim}{K}_e$ is given as

$$\underset{\sim}{K}_e = \underset{\sim}{K}_L + \underset{\sim}{K}_s \tag{26}$$

where

$$\underset{\sim}{K}_s = \underset{\sim}{G}^T\, \underset{\sim}{H}^{-1}\, \underset{\sim}{G} \tag{27}$$

The $\underset{\sim}{K}_L$ matrix is evaluated by the 3x3x2 point integration rule while the $\underset{\sim}{K}_S$ matrix associated with the higher order assumed strain is evaluated by the 4x4x2 point integration rule. Note that the $\underset{\sim}{K}_L$ matrix is in fact the same element stiffness matrix derived from the conventional assumed displacement model based on the principle of virtual work with the 3x3x2 point reduced integration rule. The $\underset{\sim}{K}_L$ matrix has spurious kinematic modes, and these modes are suppressed by adding a properly constructed $\underset{\sim}{K}_S$ matrix. Thus, $\underset{\sim}{K}_S$ plays the role of a stabilization matrix.

To construct the element stiffness matrix, it is necessary to evaluate the $\underset{\sim}{B}$ matrix at both the higher order integration points and the lower order integration points. Alternately $\underset{\sim}{B}$ at the lower order integration points can be interpolated from $\underset{\sim}{B}$ evaluated at the higher order integration points as follows:

$$\underset{\sim}{B}\,(\xi_i,\, \eta_i,\zeta_i) \;=\sum_{j=1}^{32} \tilde{N}_j(\xi_i,\eta_i,\zeta_i)\; \underset{\sim}{B}(\xi_j,\eta_j,\zeta_j) \tag{28}$$

where the subscripts i and j stand for the lower order integration points and the higher order integration points respectively, and the shape function $\tilde{N}_j$ is bicubic in ξ, η and linear in ζ such that $\tilde{N}_j = 1$ at the point j of the 4x4x2 higher order integration points and zero at other points.

CONTROL OF THE SPURIOUS KINEMATIC MODES

For an element of flat rectangular shape with sides along $x = \pm 1$ and $y = \pm 1$ lines, it is possible to determine the analytical expressions for the spurious kinematic modes of the $\underset{\sim}{K}_L$ matrix by expressing the assumed u, v, w, θ_1 and θ_2 as polynomial functions in x and y coordinates. For example, we may write

$$u = a_1 + a_2x + \cdots\cdots + a_{16}x^3y^3 \tag{29}$$

and similarly for v, w, θ_1 and θ_2. Then displacement-dependent strain vector $\underset{\sim}{\bar{E}}$ can be expressed from these assumed displacement fields. Now noting that spurious kinematic modes of the $\underset{\sim}{K}_L$ matrix do not produce strain, we set

$$\underset{\sim}{\bar{E}} = 0 \tag{30}$$

at the 3x3x2 lower order integration points. This leads to a set of 72 homogeneous equations from which we can identify the following seven spurious kinematic modes:

$$\begin{aligned} (1) \qquad u &= -C_1\, y\,(3x^2 - 5x^2y^2 + y^2) \\ v &= C_1\, x\,(x^2 - 5x^2y^2 + 3y^2) \end{aligned} \tag{31a}$$

$$\begin{aligned} (2) \qquad \theta_1 &= C_5\, x\,(-\tfrac{3}{5} + x^2 - 5x^2y^2 + 3y^2) \\ \theta_2 &= C_5\, y\,(-\tfrac{3}{5} + 3x^2 - 5x^2y^2 + y^2) \end{aligned} \tag{31b}$$

$$(3) \qquad u = C_2\, xy\,(9 - 15x^2 - 15y^2 + 25x^2y^2) \tag{31c}$$

$$(4) \qquad v = C_3\, xy\,(9 - 15x^2 - 15y^2 + 25x^2y^2) \tag{31d}$$

$$(5) \qquad w = C_4\, xy\,(9 - 15x^2 - 15y^2 + 25x^2y^2) \tag{31e}$$

$$(6) \qquad \theta_1 = C_6\, xy\,(9 - 15x^2 - 15y^2 + 25x^2y^2) \tag{31f}$$

$$(7) \qquad \theta_2 = C_7\, xy\,(9 - 15x^2 - 15y^2 + 25x^2y^2) \tag{31g}$$

where C_1, C_2, ..., C_7 are arbitrary constants. The modes given in Eqs. (31a) and (31b) are incompatible. That is, they disappear for an assembly of only two elements. However, the remaining modes are compatible and persist even after assembling elements, resulting in an unstable finite element model. These spurious kinematic modes are suppressed by introducing carefully chosen higher order assumed strain fields as follows:

The displacement-dependent strain component corresponding to Eqs. (31a) to (31g) are

$$\begin{aligned} \bar{E}_{xx} &= -C_1\,(6xy - 10xy^3) + C_5\, z(6xy - 10xy^3) \\ &\quad + C_2\,(9y - 45x^2y - 15y^3 + 75x^2y^3) \\ &\quad + C_7\, z(9y - 45x^2y - 15y^3 + 75x^2y^3) \end{aligned} \tag{32a}$$

$$\bar{E}_{yy} = C_1 (6xy - 10x^3y) - C_5 z(6xy - 10x^3y)$$
$$+ C_3 (9x - 15x^3 - 45xy^2 + 75x^3y^2)$$
$$- C_6 z(9x - 15x^3 - 45xy^2 + 75x^3y^2) \qquad (32b)$$

$$\bar{E}_{xy} = C_2 (9x - 15x^3 - 45xy^2 + 75x^3y^2)$$
$$+ C_3 (9y - 45x^2y - 15y^3 + 75x^2y^3)$$
$$+ C_7 z(9x - 15x^3 - 45xy^2 + 75x^3y^2)$$
$$- C_6 z(9y - 45x^2y - 15y^3 + 75x^2y^3) \qquad (32c)$$

$$\bar{E}_{yz} = C_4 (9x - 15x^2 - 45xy^2 + 75x^3y^2)$$
$$- C_5 (-\tfrac{3}{5} x + x^3 - 5x^3y^2 + 3xy^2)$$
$$- C_6 (9xy - 15x^3y - 15xy^3 + 25x^3y^3) \qquad (32d)$$

$$\bar{E}_{zx} = C_4 (9y - 45x^2y - 15y^3 + 75x^2y^3)$$
$$+ C_5 (-\tfrac{3}{5} y + 3x^2y - 5x^2y^3 + y^3)$$
$$+ C_7 (9xy - 15x^3y - 15xy^3 + 25x^3y^3) \qquad (32e)$$

Examining Eqs. (32a) to (32e), we realize that the spurious kinematic modes in Eqs. (31a) to (31g) are suppressed for the following higher order assumed strain fields:

$$(E_{xx})_H = \alpha_1 x^2y^3 + \alpha_5 zx^2y^3 + \alpha_7 xy^3 + \alpha_8 zxy^3$$

$$(E_{yy})_H = \alpha_2 x^3y^2 + \alpha_6 zx^3y^2 + \alpha_9 x^3y + \alpha_{10} zx^3y$$

$$(E_{xy})_H = 0 \qquad (33)$$

$$(E_{yz})_H = \alpha_3 x^3y^2$$

$$(E_{zx})_H = \alpha_4 x^2y^3$$

In Eq. (33), α_1, α_2, ····· α_{10} are unknown coefficients. Alternately, noting that the modes corresponding to C_1 and C_5 are incompatible, we may drop α_7 α_8, α_9 and α_{10} terms from Eq. (33). This leads to an assumed higher order strain field with six coefficients and the resulting element stiffness matrix has eight zero eigenvalues. However, when elements are assembled, the resulting finite element model is kinematically stable.

For an element with arbitrary geometry, we use $\xi^2\eta^3$, $\xi^3\eta^2$ terms etc. instead of x^2y^3, x^3y^2 terms etc. Since $\xi^2\eta^3$ and $\xi^3\eta^2$ are not symmetric with respect to parent coordinates ξ and η, the element stiffness matrix may be dependent on the choice of local coordinate systems used. If the local coordinate system is chosen such that the $\underset{\sim}{a}_1$ or x axis is parallel with the ξ coordinate, then the element stiffness matrix is not invariant when element geometry is nonrectangular. For example, consider the distorted elements with different node numberings as shown in Fig. 2. Even though both elements have the same geometry, we obtain two different element stiffness matrices. The local coordinate system with x or $\underset{\sim}{a}_1$ parallel with ξ has been used in Lee, Wong and Rhiu (1985) in conjunction with a nine node shell element. In spite of the lack of invariance of the element stiffness matrices, this nine node shell element showed excellent performance. This indicates that the invariance property is not absolutely necessary for a good finite element. However, in the present study, we enforce the invariance of element stiffness matrices by assigning a particular local coordinate system for a given geometry of elment as follows [Rhiu and Lee (1987)]:

If $\underset{\sim}{X}_0$ denotes the position vector of the point located at $\xi = \eta = \zeta = 0$, we may define two unit vectros $\underset{\sim}{v}_1$ and $\underset{\sim}{v}_2$ at this point such that

$$\underset{\sim}{v}_1 = \frac{\partial \underset{\sim}{X}_o}{\partial \xi} \Big/ \left| \frac{\partial \underset{\sim}{X}_o}{\partial \xi} \right| \tag{34a}$$

$$\underset{\sim}{v}_2 = \frac{\partial \underset{\sim}{X}_o}{\partial \eta} \Big/ \left| \frac{\partial \underset{\sim}{X}_o}{\partial \eta} \right| \tag{34b}$$

The angle θ_o between these two unit vectors is determined by the following equation,

$$\cos \theta_o = \underset{\sim}{v}_1 \cdot \underset{\sim}{v}_2 \tag{35}$$

Then, if θ_o is less than or equal to 90°, the unit vector $\underset{\sim}{a}_1$ in the x direction of local coordinate system is chosen to be parallel to ξ axis such that

$$\underset{\sim}{a}_1 = \frac{\partial \underset{\sim}{X}_o}{\partial \xi} \Big/ \left| \frac{\partial \underset{\sim}{X}_o}{\partial \xi} \right| \tag{36a}$$

Otherwise, $\underset{\sim}{a}_1$ is parellel to n axis such that

$$\underset{\sim}{a}_1 = \frac{\partial \underset{\sim}{X}_o}{\partial \eta} \Big/ \left| \frac{\partial \underset{\sim}{X}_o}{\partial \eta} \right| \tag{36b}$$

With this choice of $\underset{\sim}{a}_1$, we can easily determine the other two unit vectors $\underset{\sim}{a}_2$ and $\underset{\sim}{a}_3$, with $\underset{\sim}{a}_3$ being normal to the shell midsurface. Note that, while $\underset{\sim}{v}_1$ and $\underset{\sim}{v}_2$ are determined at $\xi = \eta = \zeta = 0$ point, the $\underset{\sim}{a}_1$, $\underset{\sim}{a}_2$ and $\underset{\sim}{a}_3$ vectors can be computed at any point on the shell midsurface. In particular, $\underset{\sim}{a}_1$, $\underset{\sim}{a}_2$ and $\underset{\sim}{a}_3$ are needed at the integration points.

With the local coordinate system defined as above, the higher order assumed strains for the sixteen node shell element are chosen as follows:

$$\overline{\underset{\sim}{E}}_H = \underset{\sim}{P}\, \underset{\sim}{\alpha} \tag{37}$$

where for the 10α version,

$$\underset{\sim}{P} = \begin{bmatrix} f_1 & 0 & \zeta f_1 & 0 & 0 & 0 & f_2 & 0 & \zeta f_2 & 0 \\ 0 & g_1 & 0 & \zeta g_1 & 0 & 0 & 0 & g_2 & 0 & \zeta g_2 \\ 0 & 0 & 0 & 0 & 0 & 0 & 0 & 0 & 0 & 0 \\ 0 & 0 & 0 & 0 & g_1 & 0 & 0 & 0 & 0 & 0 \\ 0 & 0 & 0 & 0 & 0 & f_1 & 0 & 0 & 0 & 0 \end{bmatrix} \tag{38a}$$

$$\underset{\sim}{\alpha} = \lfloor \alpha_1, \alpha_2, \ldots, \alpha_{10} \rfloor^T \tag{38b}$$

and for the 6α version,

$$\underset{\sim}{P} = \begin{bmatrix} f_1 & 0 & \zeta f_1 & 0 & 0 & 0 \\ 0 & g_1 & 0 & \zeta g_1 & 0 & 0 \\ 0 & 0 & 0 & 0 & 0 & 0 \\ 0 & 0 & 0 & 0 & g_1 & 0 \\ 0 & 0 & 0 & 0 & 0 & f_1 \end{bmatrix} \tag{39a}$$

$$\underset{\sim}{\alpha} = \lfloor \alpha_1, \alpha_2, \ldots, \alpha_6 \rfloor^T \tag{39b}$$

In Eqs. (38a) and (39a), f_1, f_2, g_1, and g_2 are chosen as follows:

(1) if x or $\underset{\sim}{a}_1$ is parallel to ξ as in Eq. (36a)

$$f_1 = \xi^2\eta^3, \quad f_2 = \xi\eta^3 \tag{40a}$$

$$g_1 = \xi^3\eta^2, \quad g_2 = \xi^3\eta \tag{40b}$$

(2) if x or $\underset{\sim}{a}_1$ is parallel to η as in Eq. (36b)

$$f_1 = \xi^3\eta^2, \quad f_2 = \xi^3\eta \tag{41a}$$

$$g_1 = \xi^2\eta^3, \quad g_2 = \xi\eta^3 \tag{41b}$$

NUMERICAL TESTS

In order to evaluate the performance of the present sixteen node element, several numerical tests involving simple plates and shells were carried out. For the purpose of identification, the present sixteen node element is called

SHEL16. Whenever possible, the effectiveness of SHEL16 element is compared with the DISP16 element based on the conventional displacement model with the 4x4x2 point integration rule. Most of the numerical results are presented in tabular form so that they can be used for future reference. For the SHEL16 element, it turns out that numerical results for the 6α assumed strain and the 10α assumed strain are almost identical for the cases tested in this paper. Therefore only the results for the 6α version is presented. All numerical examples were calculated with double precision accuracy on the UNIVAC 1100/92 machine at the University of Maryland.

(a) A Simply Supported or Clamped Square Plate

Plate bending problems provide examples to investigate the effect of transverse shear locking alone. A quarter of a square plate subjected to uniformly distributed load p was modeled by uniform 1x1 and 2x2 meshes and distorted 2x2 and 4x4 meshes as shown in Figs. 3(a) to 3(c). Both simply supported and clamped boundary conditions were considered.

Table 1 lists the computed nondimensional deflection at the centroid of the plate. These values are normalized with respect to the analytical solution based on the Kirchhoff thin plate theory [Timoshenko and Woinowski-Krieger (1959)]. For the simply supported plate, both SHEL16 and DISP16 elements give numerical results very close to the analytical solutions for the uniform meshes. For the distorted 2x2 mesh, the SHEL16 element does not suffer any transverse shear locking over a wide range of L/t ratios while the DISP16 element reveals a slight effect of shear locking when the plate becomes very thin. For the distorted 4x4 mesh, both elements give very accurate results. For the clamped plate, the SHEL16 element gives very accurate and reliable numerical results over a wide range of L/t ratios regardless of mesh distortion. However, for the distorted meshes, the performance of the DISP16 element deteriorates as

the plate becomes thin. Even in this case, the 4x4 mesh shows very accurate solution up to L/t = 10,000.

Table 2 shows nondimensional bending moments M_x/pL^2 per unit length evaluated at integration point E and nondimensional shear forces Q_x/pL per unit length evaluated at integration point F. Note that the SHEL16 element solutions are totally insensitive to the wide range of L/t ratios considered here. Table 2 also includes analytical solutions obtained at corner points C and D. They are listed to check the order of magnitude of numerical solutions.

(b) A Pinched Cylindrical Shell

As a deep shell example, a cylindrical shell loaded at two opposite points as shown in Fig. 4 was tested. Both diaphragmed and fixed edge conditions were considered. Due to symmetry in geometry and loading, only one octant of the shell was modeled by 3x4, 4x5 and 5x6 meshes as shown in Figs. 5(a)-(c). In addition, as shown in Fig. 5(d), an irregular mesh designated as 5x6I was also considered. Note that the meshes illustrated in Figs. 5(a)-(d) are on the stretched plane of the octant ABCD of the shell. Moreover, in order to describe more accurately the complex shell behavior in the region near the load point C, fine meshes are used along lines BC and CD.

Table 3 lists the nondimensional displacements at various points on the diaphragmed shell for R/t = 100, 300 and 500. They are compared with the analytical solutions given by Flügge (1962). The analytical solution is based on a shell theory which neglects the effect of transverse shear deformation. Table 3 also includes numerical results obtained by the DISP16 element with the 5x6 mesh. For the models with SHEL16 elements, the solutions get closer to the analytical solutions as the number of elements increases. It is noteworthy that the solutions for the distorted 5x6I mesh are very close to that for the regular 5x6 mesh. On the other hand, the DISP16 element shows signs of locking as the solutions deteriorate with increasing R/t ratios. Even for R/t = 100, the 5x6

mesh solution with the DISP16 element is worse than the 3x4 mesh solution with the SHEL16 element.

Table 4 lists nondimensional deflections at the pinched point C of the shell with fixed ends. A good convergence is observed as the finite element model with the SHEL16 elements is refined. Also there is no significant discrepancy between the 5x6 mesh and the 5x6I mesh. Figs. 6 and 7 show inplane force N_1 and moment M_2 per unit length along line BC for the 5x6 mesh with SHEL16 elements. An analytical solution for the fixed ends case is not available.

(c) A Hemispherical Shell

As a doubly curved shell example, a hemispherical shell subjected to concentrated loads as shown in Fig. 8 was considered. This problem exhibits predominantly bending behavior with very little inplane behavior. Due to symmetry in geometry and loading, a quarter of the shell was modeled by 4 element, 9 element, 16 element and 20 element meshes. The 4 element, 9 element and 16 element meshes are created by dividing uniformly over the angles θ and ϕ. The 20 element mesh is created from the 16 element mesh as shown in Fig. 8.

For convenience, a small region at point C was not included in the finite element modeling. As a check, two different cases were tested. In one case, the region within $\theta = 0.5°$ was cut out while, in the other case, the region within $\theta = 1°$ was excluded. The two cases gave the same result. In table 5 the computed nondimensional deflection DW_A/PR^2 at point A is compared with the analytical solution reported by Morley and Morris (1978). Symbol D represents bending rigidity. The analytical solution is based on the Rayleigh-Ritz method. For $R/t = 250$, the solution for the 16 element model agrees exactly with the analytical value of 0.185. Even the 10 element model shows only 0.05% error. On the other hand, the DISP16 element suffers from locking. Table 5 also includes the $R/t = 500$ case. Morley and Morris (1978) did not consider this case.

(d) A Toroidal Shell under Internal Pressure

A toroidal shell subjected to an internal pressure p was analyzed by the SHEL16 element. Figures 9(a) and 9(b) show the geometry and material data. The toroidal shell has both positive and negative curvatures along the meridional angle. Due to the horizontal plane of symmetry and the axisymmetric loading, an upper sector of shell with an angle of 8° was modeled with a row of 13 elements and a row of 26 elements. The subtended angles of individual elements in the 13 element model are listed in Table 6. The 26 element model is obtained from the 13 element model by dividing each element into two elements with equal subtended angles. Numerical results for the 13 element model and the 26 element model were almost the same. Therefore only the 13 element solutions are reported here.

Table 7 shows nondimensional normal deflection $(w/r) \times 10^3$ in comparison with the numerical solution by Kalnins (1964) for r/t ratios of 20 and 200. Kalnins' solution is a combination of the direct integration and the finite difference method. A very good agreement between the results of the SHEL16 element and Kalnins' solution is observed. Table 7 also includes the SHEL16 element solution for r/t = 1,000. This case was not considered by Kalnins. Figures 10 and 11 show the deflection and the bending stress $(\sigma_{\theta\theta})_b$ at the top surface of the shell along the meridional angle direction. An excellent agreement between the two solutions is observed for r/t = 20 and 200. For r/t = 200, the distribution of the membrane stress $(\sigma_{\theta\theta})_m$ is shown in Fig. 12. Again the SHEL16 element solution is almost identical to Kalnins' solution. The $(\sigma_{\theta\theta})_m/E$ curves for r/t = 20 and 1,000 are very close to that for r/t = 200. Therefore, they are not shown in Fig. 12 to avoid cluttering.

CONCLUSION

Results of numerical tests demonstrate that the present SHEL16 element

can be used to provide reliable solutions for thin plates and shells regardless of distorted element geometries and clamped boundary conditions. In addition, the SHEL16 element with the 10α version assumed strain is kinematically stable at element level while the SHEL16 element with the 6α version assumed strain is kinematically unstable at element level but stable at global structural level. Thus the stabilization scheme with a judiciously chosen set of higher order assumed strain terms has successfully suppressed compatible kinematic modes without reintroducing the locking effect. Finally, the present SHEL16 element can be used to generate benchmark solutions for testing the performance of other shell elements.

ACKNOWLEDGEMENT

The authors express their deep appreciation of the support for the present work provided by the Office of Naval Research (ONR Contract No. N00014-84-K-0385).

REFERENCES

Ahmad, S.; Irons, B.M.; Zienkiewicz, O.C. (1970): Analysis of thick and thin shell structures by curved elements. Int. J. Num. Meth. Engng. 2, 419-451.

Belytschko, T.; Liu, W.K.; Ong, J.S.J.; Lam, D. (1985): Implementation and application of a 9-node Lagrangian shell element with spurious mode control. Computers and Structures 20, 121-128.

Belytschko, T.; Ong, J.S.J. ; Liu, W.K. (1984): A consistent control of spurious singular modes in the 9-node Lagrange element for the Laplace and Mindlin plate equations. Comp. Meth. App. Mech. Engng. 44, 269-295.

Flügge, W. (1962) Stresses in shells. Berlin; Springer-Verlag.

Fraejis de Veubeke, B. (1965): Displacement and equilibrium models in the finite element method. In: Zienkiewicz, O.C.; Holister, G.S.(eds): Stress analysis, London: Wiley

Hughes, T.J.R.; Cohen, M.; Haroun, M. (1978): Reduced and selective integration techniques in the finite element analysis of plates. Nuclear Engng. Design 46, 203-222.

Kalnins, A. (1964): Analysis of shells of revolution subjected to symmetric and nonsymmetric loads. J. Appl. Mech. 86, 467-476.

Lee, S.W. (1978): Finite element methods for reduction of constraints and creep analysis. Ph.D. dissertation, Dept. Aero. and Astro., MIT.

Lee, S.W.; Pian, T.H.H. (1978): Improvement of plate and shell finite elements by mixed formulations. AIAA J. 16, 29-34.

Lee, S.W.; Rhiu, J.J (1986): A new efficient approach to the formulation of mixed finite element models for structural analysis. Int. J. Num. Meth. Engng. 22, 1629-1641.

Lee, S.W.; Wong, S.C.; Rhiu, J.J. (1985): Study of a nine-node mixed formulation finite element for thin plates and shells. Computers and Structures 21, 1325-1334.

Malkus, D.S.; Hughes, T.J.R. (1978): Mixed finite element methods - Reduced and selective integration techniques: A unification of concepts. Comp. Meths. Appl. Mech. Engng. 15, 63-81.

Morley, L.S.D.; Morris, A.J. (1978): Conflict between finite elements and shell theory. In: Robinson, J. (ed): Finite element methods in the commercial environment, Vol. 2, Okehampton, U.K.

Pawsey, S.F.; Clough, R.W. (1971): Improved numerical integration of thick shell finite elements. Int. J. Num. Meth. Engng. 3, 575-586.

Pugh, E.D.L.; Hinton, E.; Zienkiewicz, O.C. (1978): A study of quadrilateral plate bending elements with reduced integration. Int. J. Num. Meth. Engng. 12, 1059-1079.

Rhiu, J.J. (1985): A new and efficient formulation for finite element analysis of thin shell structures undergoing small and large deflection. Ph.D. dissertation, Dept. of Aero. Engng., University of Maryland.

Rhiu, J.J.; Lee, S.W. (1987): A new efficient mixed formulation for thin shell finite element models. accepted for publication in Int. J. Num. Meth. Engng.

Stolarski, H.; Belytschko, T. (1982): Membrane locking and reduced integration for curved elements. J. of Applied Mechanics 49, 172-176.

Timoshenko, S.P.; Woinowsky-Krieger, S. (1959): Theory of plate and shells. 2nd Ed., New York; McGraw-Hill.

Zienkiewicz, O.C.; Too,J.; Taylor, R.L.: (1971): Reduced integration technique in general analysis of plates and shells. Int. J. Num. Meth. Engng. 3, 275-290.

Table 1. Maximum nondimensional deflection at the centroid of the square plate under uniform pressure

Plate	Mesh	Element	L/t 10^2	10^3	10^4	10^5
Simply Supported	Uniform:					
	1x1	SHEL16	1.0000	0.9995	0.9995	0.9995
		DISP16	1.0153	1.0150	1.0150	1.0150
	2x2	SHEL16	1.0005	1.0000	1.0000	1.0000
		DISP16	1.0012	1.0007	1.0007	1.0007
	Distorted:					
	2x2	SHEL16	1.0007	1.0007	1.0005	1.0005
		DISP16	1.0015	0.9956	0.9542	0.9380
	4x4	SHEL16	1.0005	1.0002	1.0002	1.0002
		DISP16	1.0000	1.0002	1.0000	0.9906
Clamped	Uniform:					
	1x1	SHEL16	0.9968	0.9945	0.9945	0.9945
		DISP16	1.0482	1.0474	1.0474	1.0474
	2x2	SHEL16	1.0024	1.0000	1.0000	1.0000
		DISP16	1.0016	1.0000	1.0000	1.0000
	Distored:					
	2x2	SHEL16	1.0024	1.0000	0.9960	0.9960
		DISP16	0.9945	0.9486	0.3007	0.0048
	4x4	SHEL16	1.0024	1.0000	1.0000	0.9992
		DISP16	1.0016	0.9992	0.9929	0.8632

Table 2. Nondimensional bending moment and shear force of the square plate (SHEL16 element with uniform 2x2 mesh)

	Simply Supported Plate		Clamped Plate	
$\frac{L}{t}$	$(\frac{M_x}{pL^2})_E$	$(\frac{Q_x}{pL})_F$	$(\frac{M_x}{pL^2})_E$	$(\frac{Q_x}{pL})_F$
10^2	0.0476	0.310	0.0226	-0.404
10^3	0.0476	0.310	0.0226	-0.404
10^4	0.0476	0.310	0.0226	-0.404
10^5	0.0476	0.310	0.0226	-0.404
Analytical	$(\frac{M_x}{pL^2})_C$	$(\frac{Q_x}{pL})_D$	$(\frac{M_x}{pL^2})_C$	
	0.0479	0.338	0.0231	

Table 3. Nondimensional displacements for the pinched cylinder with diaphragmed ends

$\frac{R}{t}$	Element	Mesh	$-\frac{Etw_C}{P}$	$-\frac{Etw_B}{P}$	$-\frac{Etu_D}{P}$
100	SHEL16	3x4	165.3	0.6776	4.102
		4x5	166.1	0.5218	4.113
		5x6	166.3	0.4770	4.113
		5x6I	166.3	0.4718	4.113
	DISP16	5x6	159.1	1.497	4.087
	Analytical		164.3	0.4693	4.114
300	SHEL16	3x4	636.3	12.52	9.778
		4x5	642.3	12.52	9.785
		5x6	646.9	12.22	9.853
		5x6I	646.5	12.32	9.853
	DISP16	5x6	531.1	21.31	9.397
	Analytical		647.3		9.867
500	SHEL16	3x4	1172.2	10.60	14.46
		4x5	1200.9	10.23	14.45
		5x6	1212.0	13.47	14.55
		5x6I	1210.2	13.21	14.54
	DISP16	5x6	847.6	5.904	13.32
	Analytical		1223.4		14.67

Table 4. Nondimensional deflection $-Etw_C/P$ at the load point C of the pinched cylindrical shell with fixed ends

	R/t		
Mesh	100	300	500
3x4	137.2	511.1	930.9
4x5	137.9	518.5	961.5
5x6	138.2	521.6	969.2
5x6I	138.2	521.2	967.4

Table 5. Nondimensional deflection $-Dw_A/PR^2$ at the point A of the hemispherical shell

R/t	Element	No. of elements 4	9	16	20
250	SHEL16	0.174	0.183	0.185	-
	DISP16	-	0.113	0.160	-
500	SHEL16	0.158	0.176	0.182	0.182
	DISP16	-	0.055	0.123	0.139

Table 6. Meridional subtended angle of the elements for the toroidal shell

element no.	1	2	3	4	5	6	7	8	9	10	11	12	13
$\Delta\theta$ (degrees)	20	20	20	11	10	7	4	7	10	11	20	20	20

Table 7. Nondimensional deflections $(w/r) \times 10^3$ of the toroidal shell

θ	r/t = 20		r/t = 200		r/t = 1000
(degrees)	SHEL16	Kalnins	SHEL16	Kalnins	SHEL16
0	0.1034	0.103	0.1038	0.100	0.1034
81	4.2119	4.208	5.1423	5.151	5.2911
99	3.4668	3.467	3.2952	3.297	2.8179
140	1.2513	1.249	1.3038	1.298	1.3273

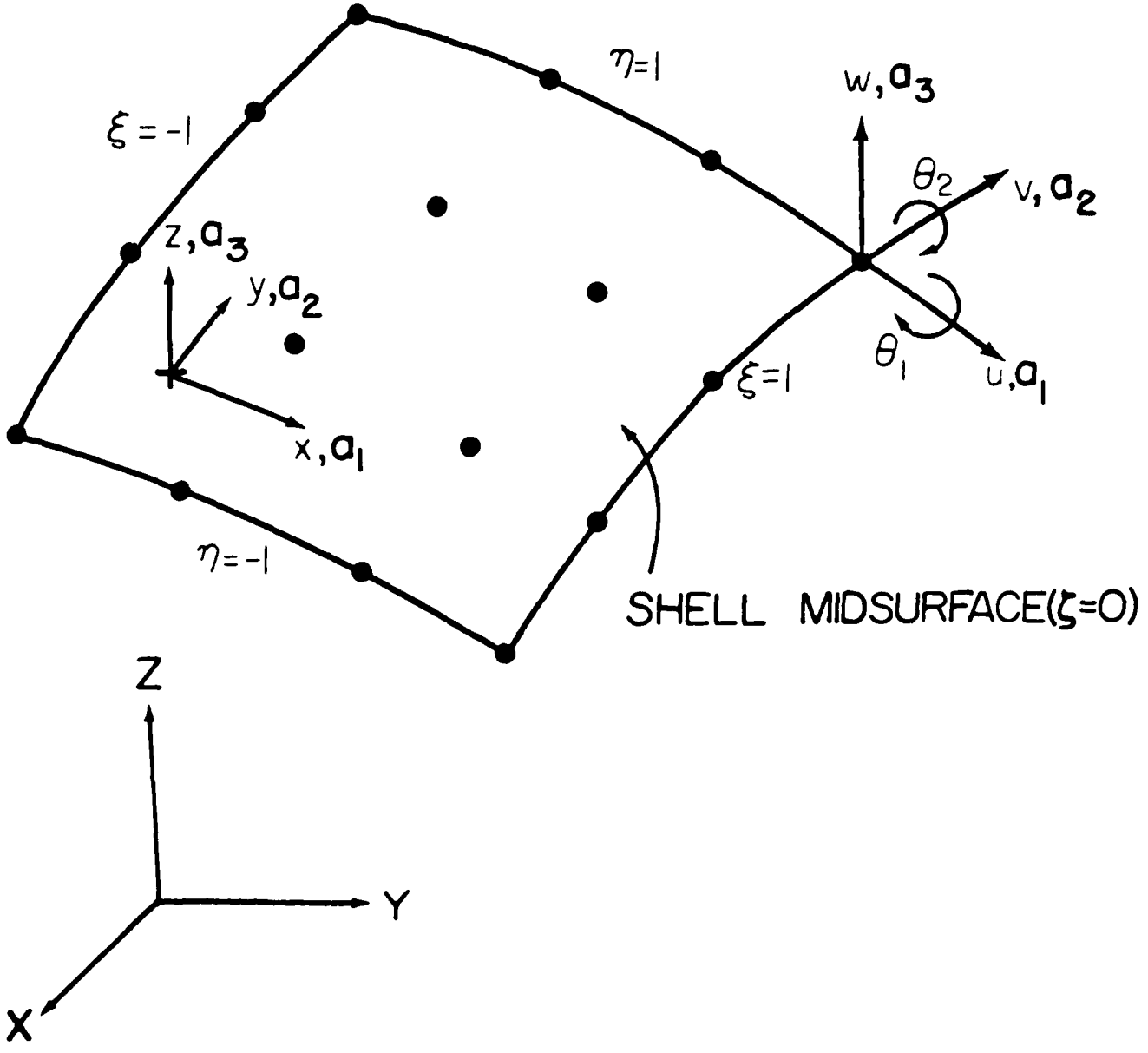

Figure 1 A sixteen node shell element

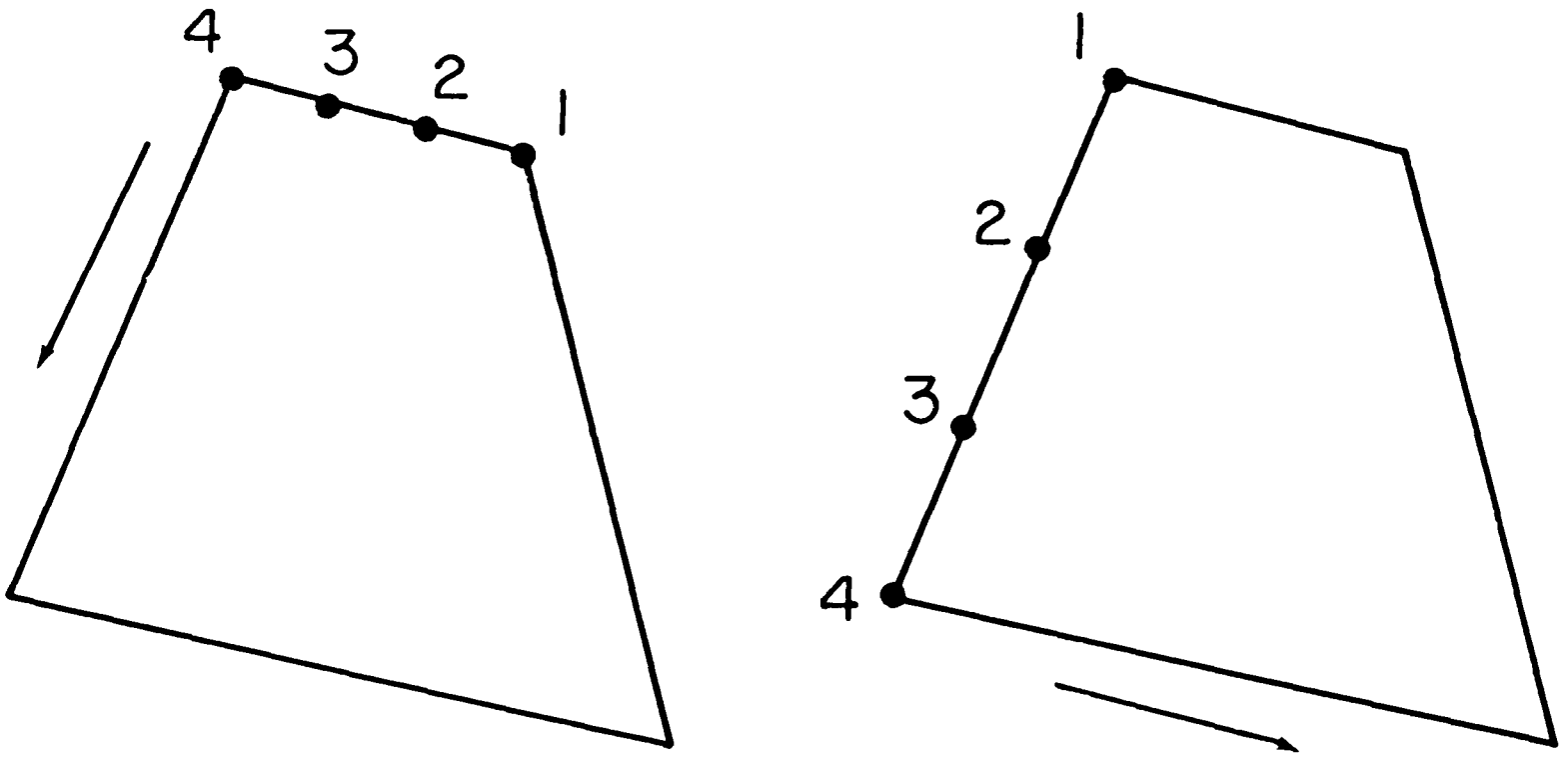

Figure 2 Two different node numbering schemes

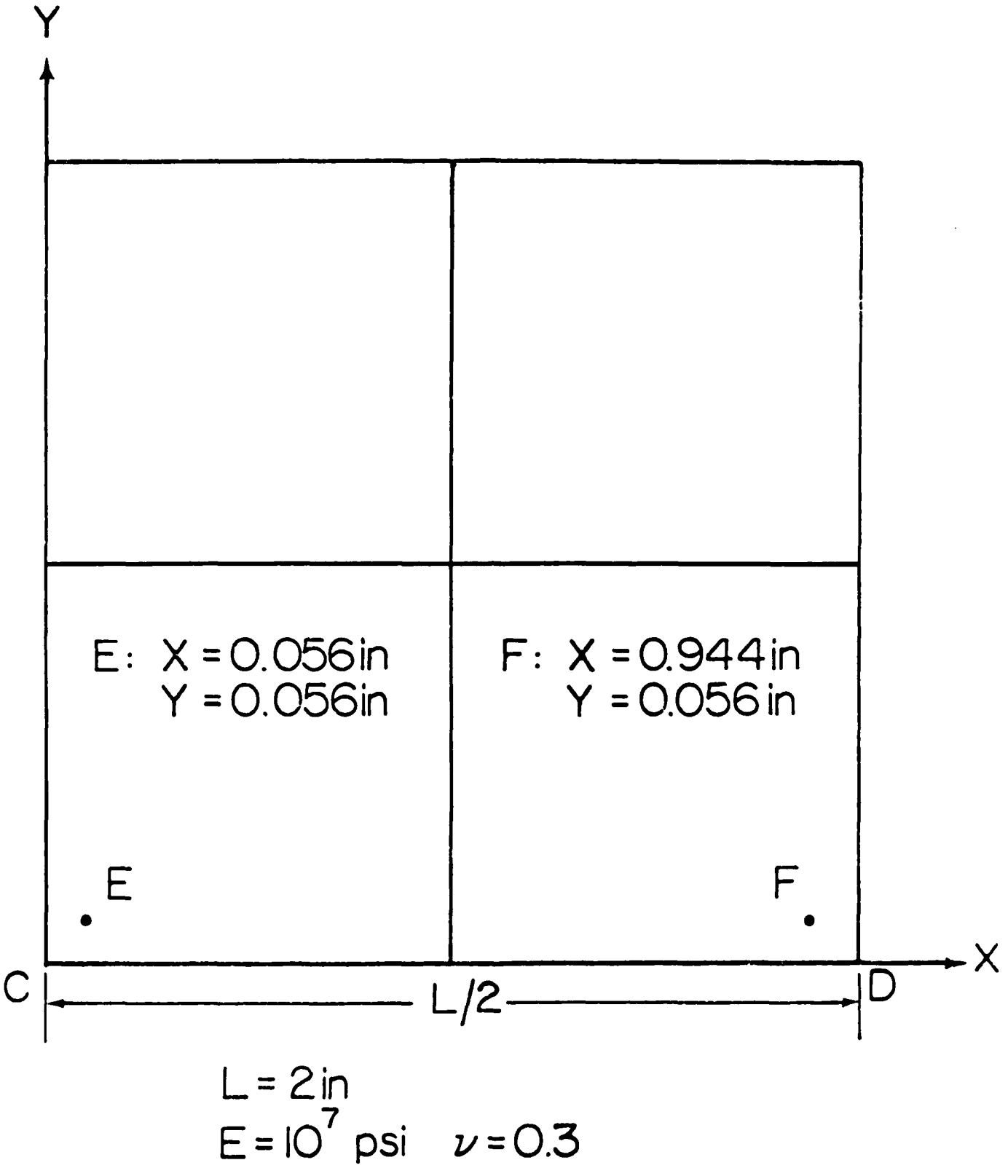

Figure 3(a) A square plate: 2x2 uniform mesh

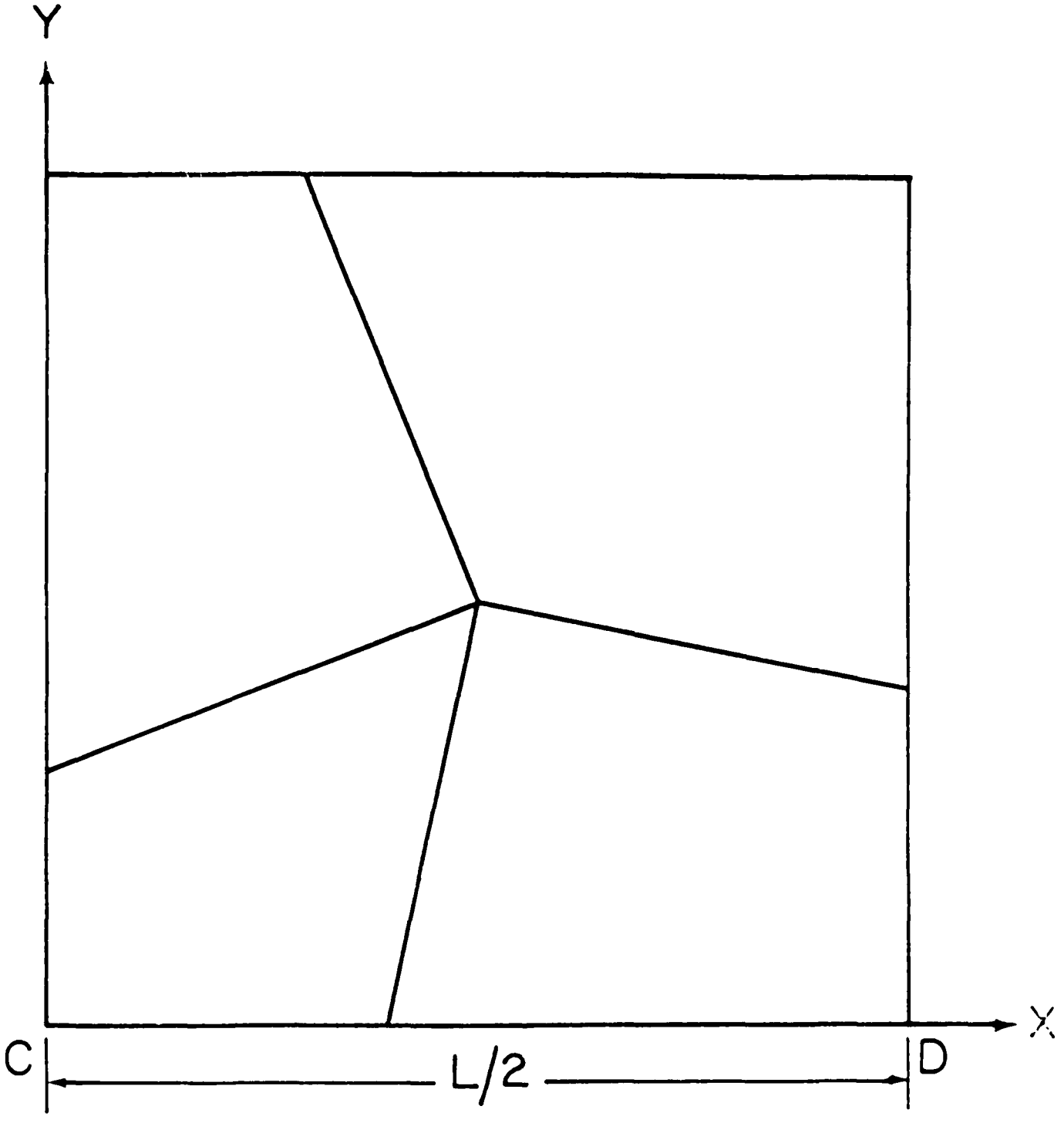

Figure 3(b) A square plate: 2x2 distorted mesh

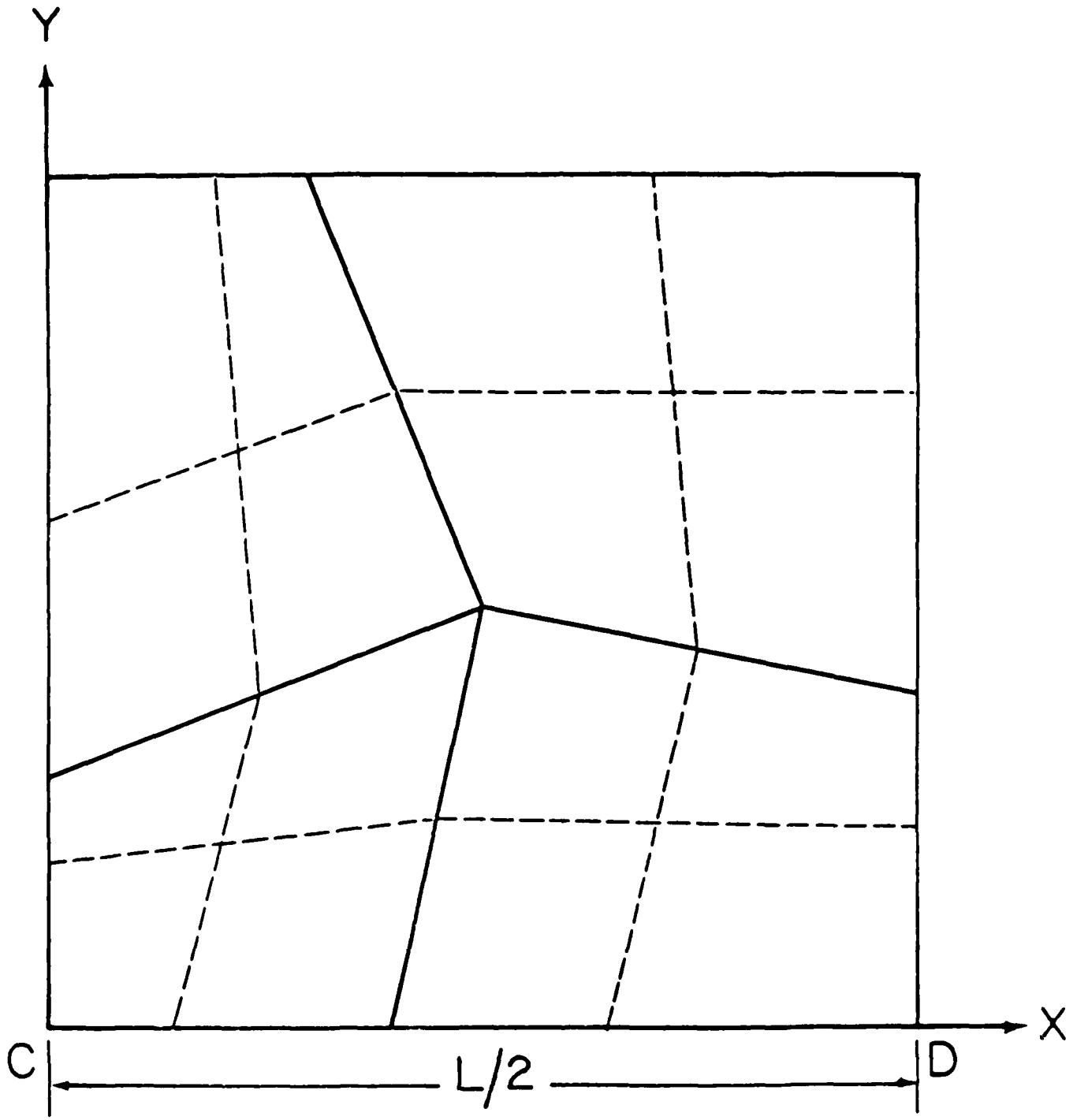

Figure 3(c) A square plate: 4x4 distorted mesh

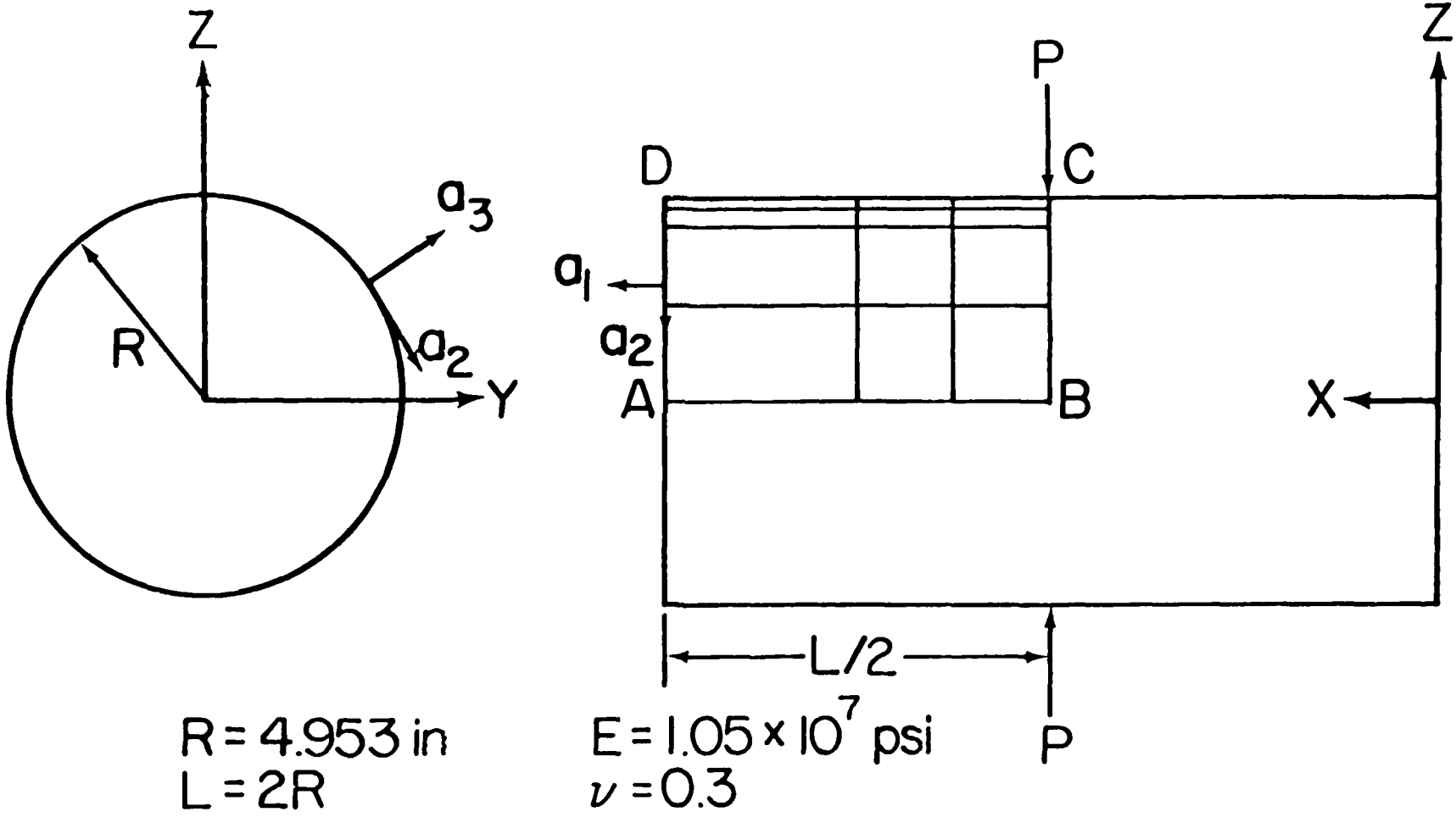

Figure 4 A pinched cylindrical shell

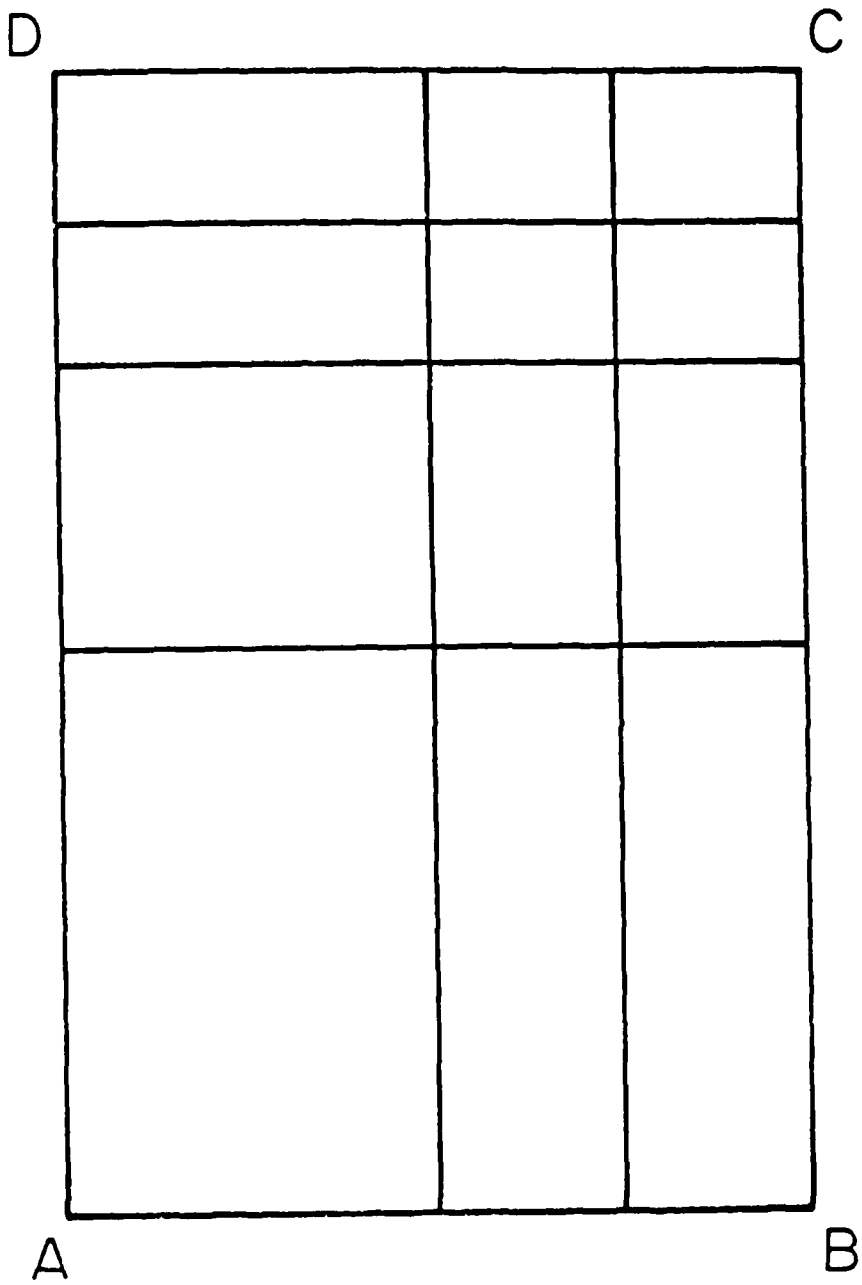

Figure 5(a) Finite element models for cylindrical shell: 3x4 mesh

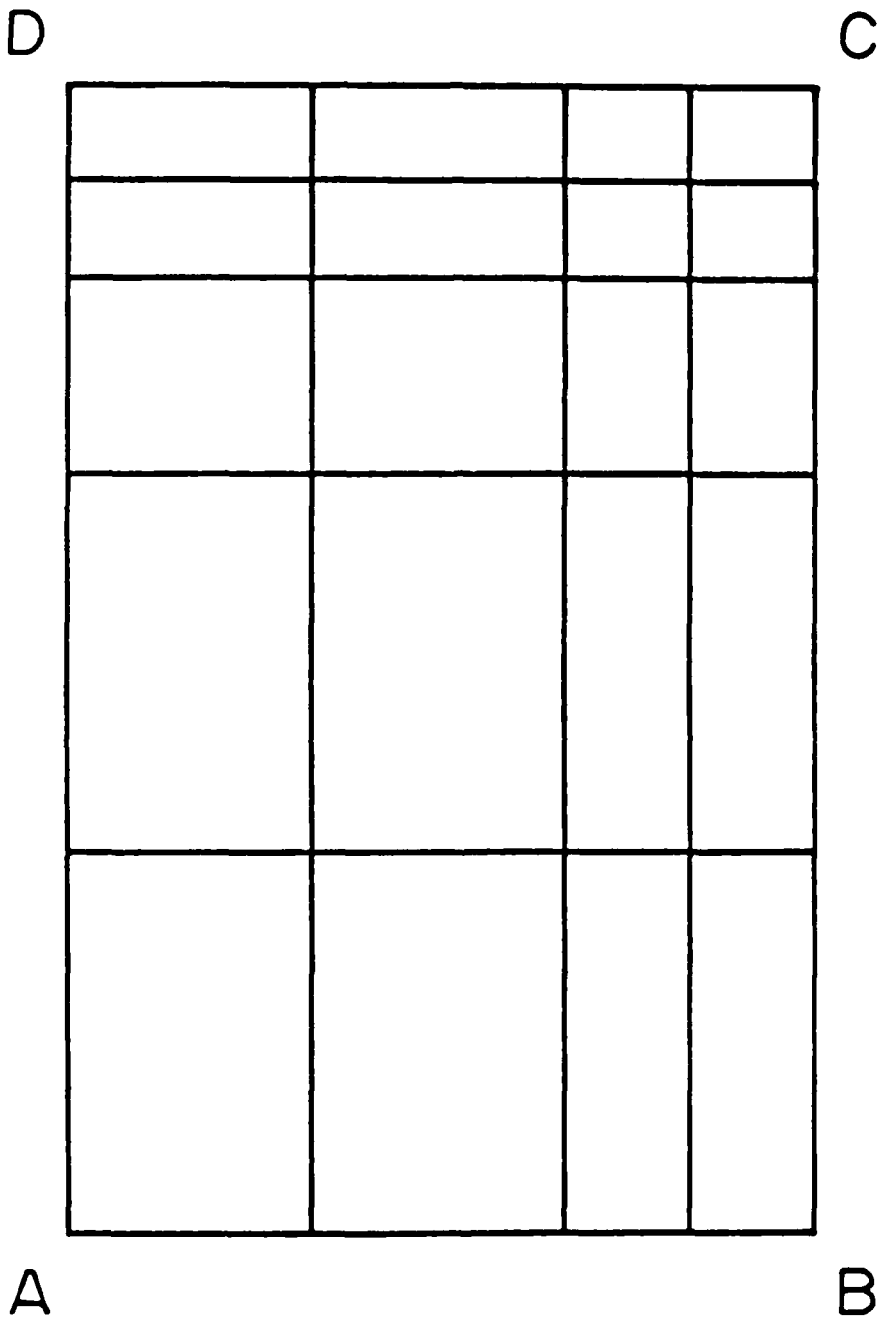

Figure 5(b) Finite element models for cylindrical shell: 4x5 mesh

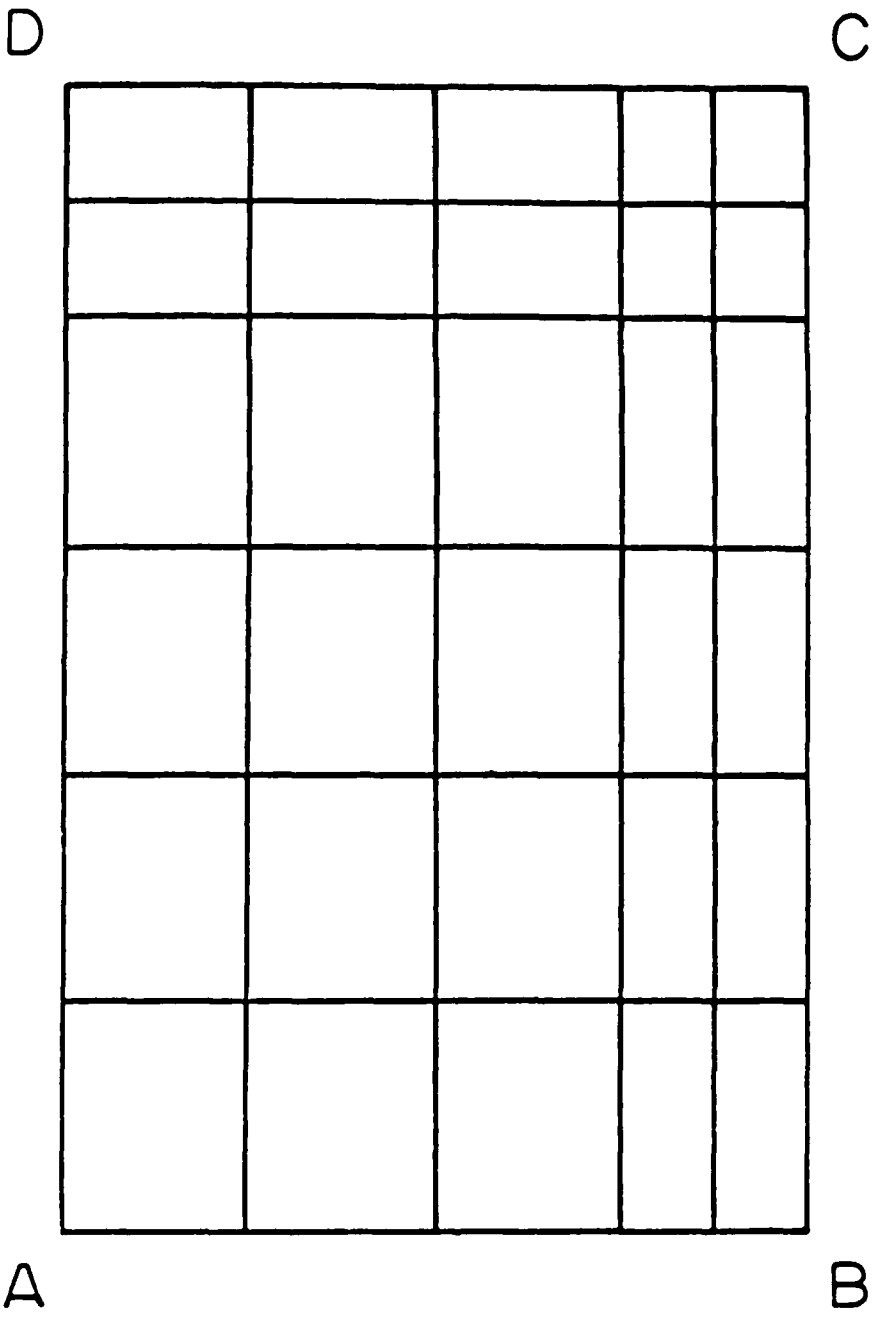

Figure 5(c) Finite element models for cylindrical shell: 5x6 mesh

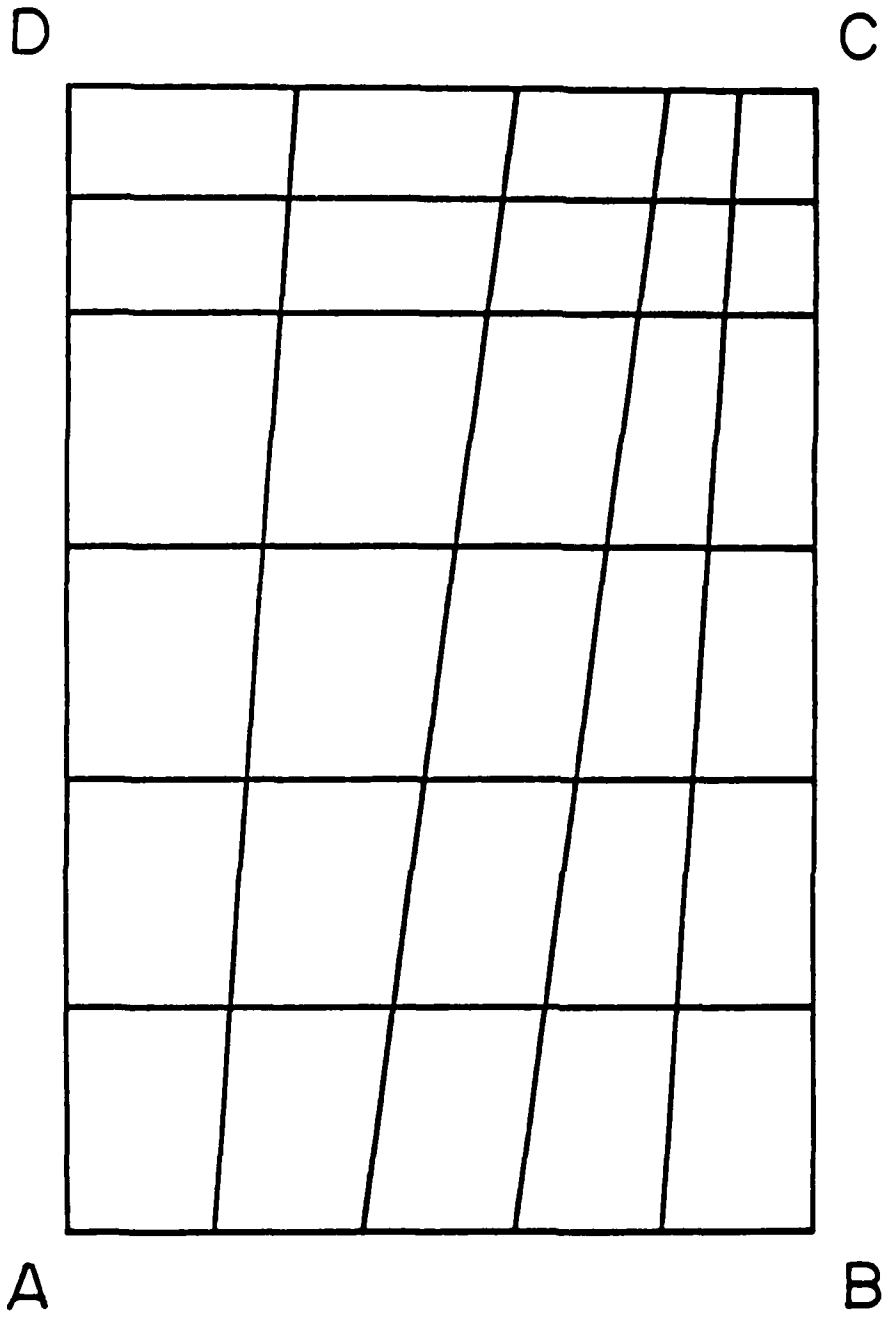

Figure 5(d) Finite element models for cylindrical shell: 5x6I mesh

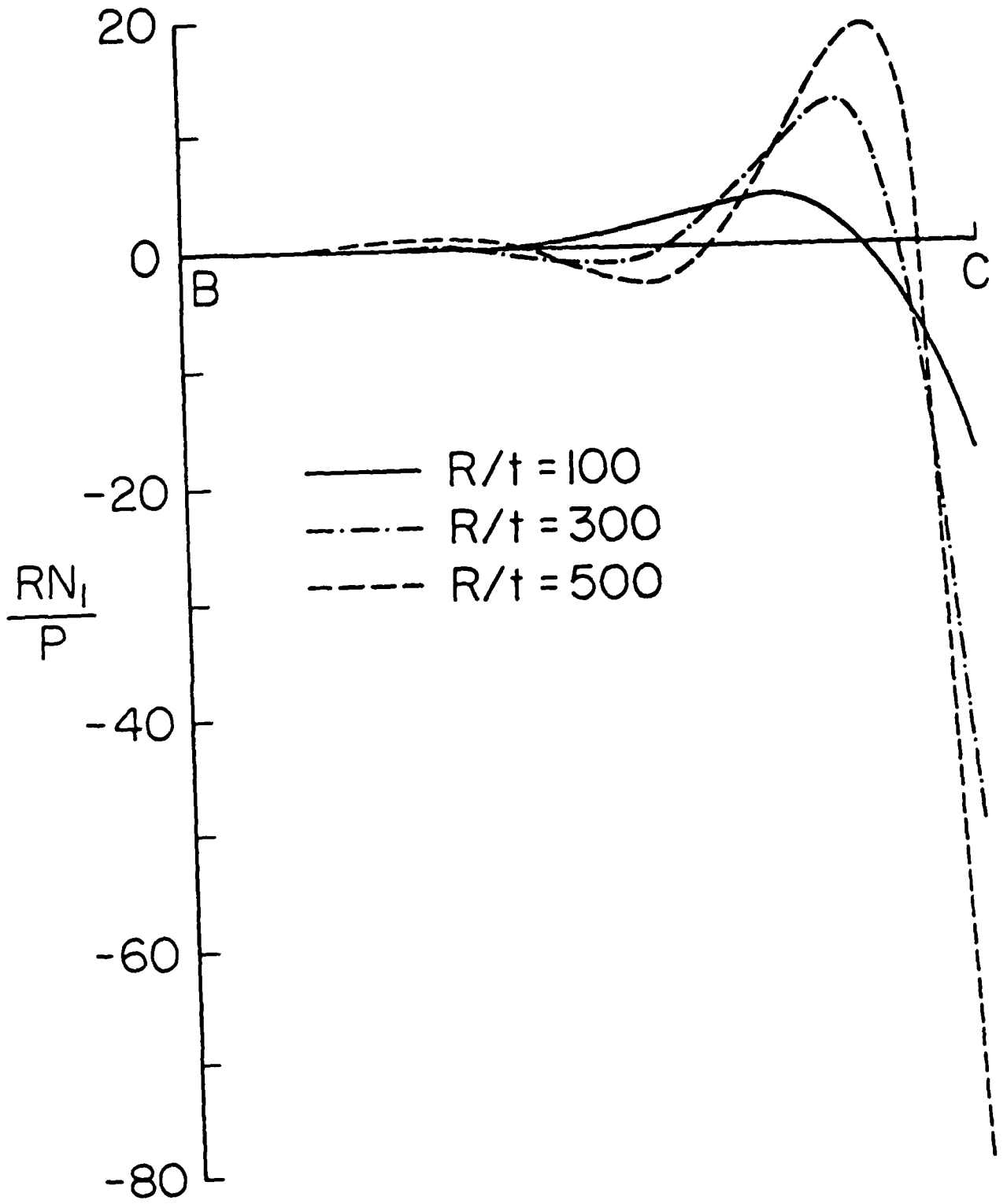

Figure 6 Inplane force along line BC of the pinched cylindrical shell with fixed ends

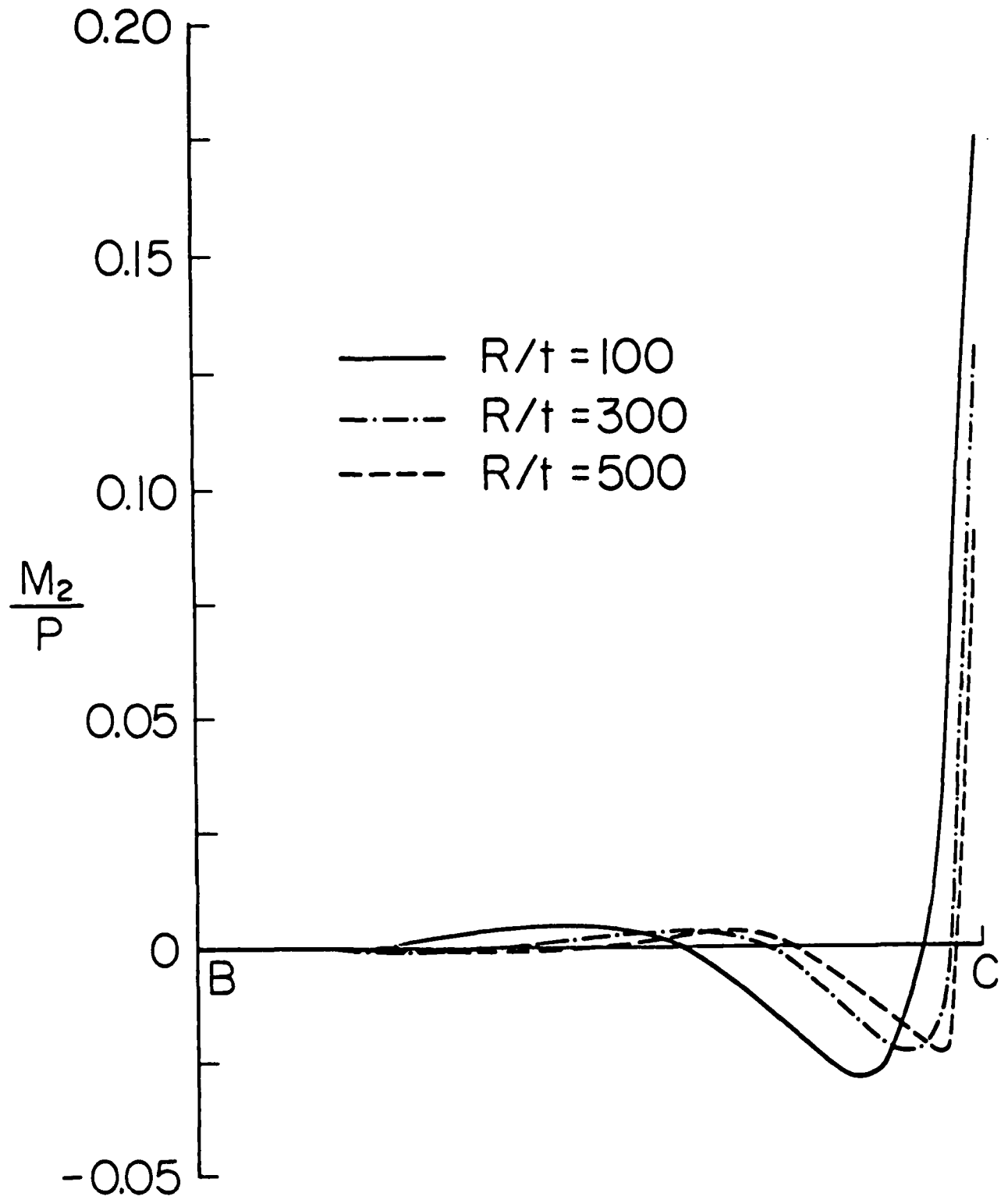

Figure 7 Bending moment distribution along line BC of the pinched cylindrical shell with fixed ends

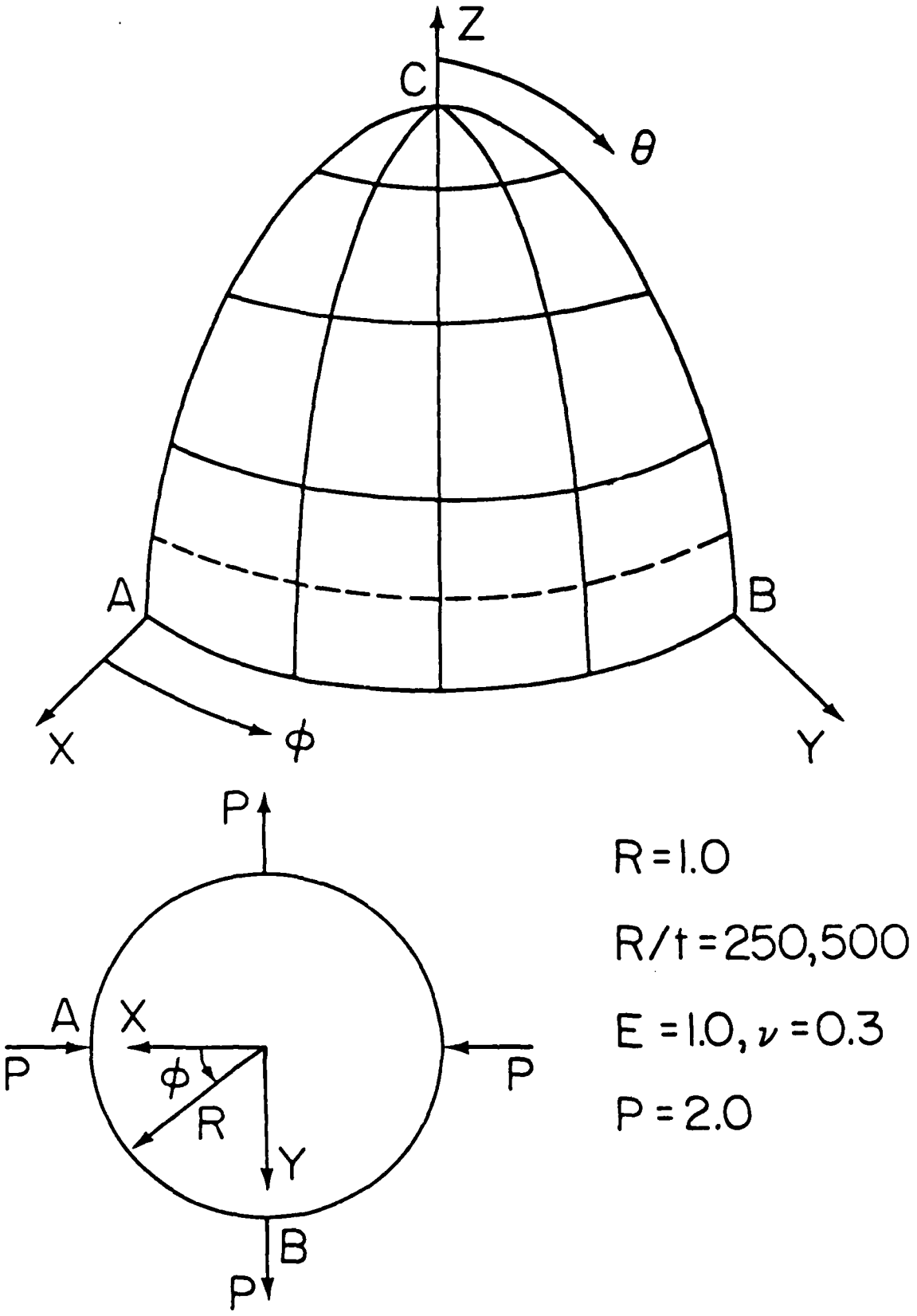

Figure 8 Finite element mesh for one quarter of the hemispherical shell subjected to concentrated loads

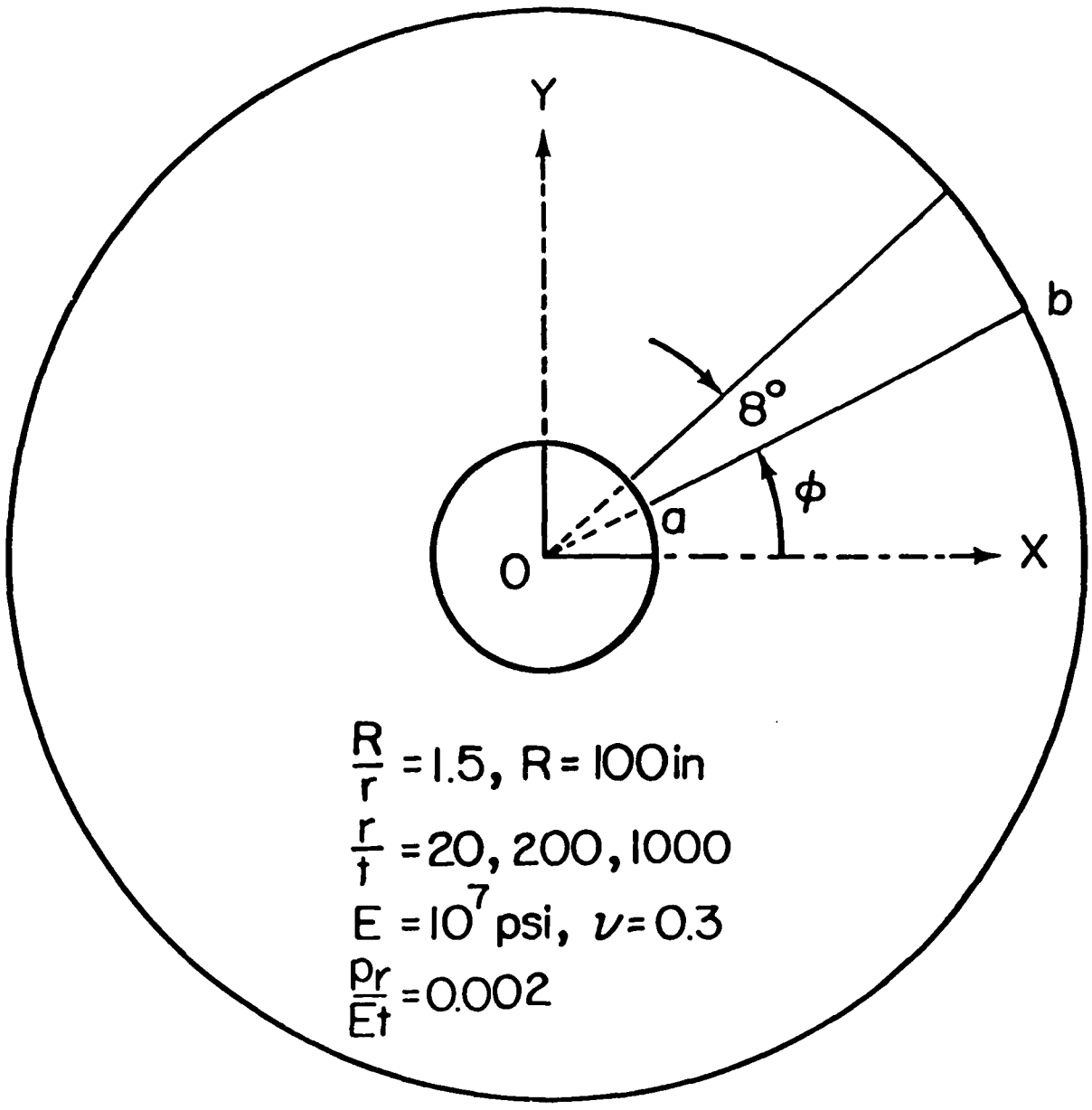

Figure 9(a) A toroidal shell under internal pressure p: top view

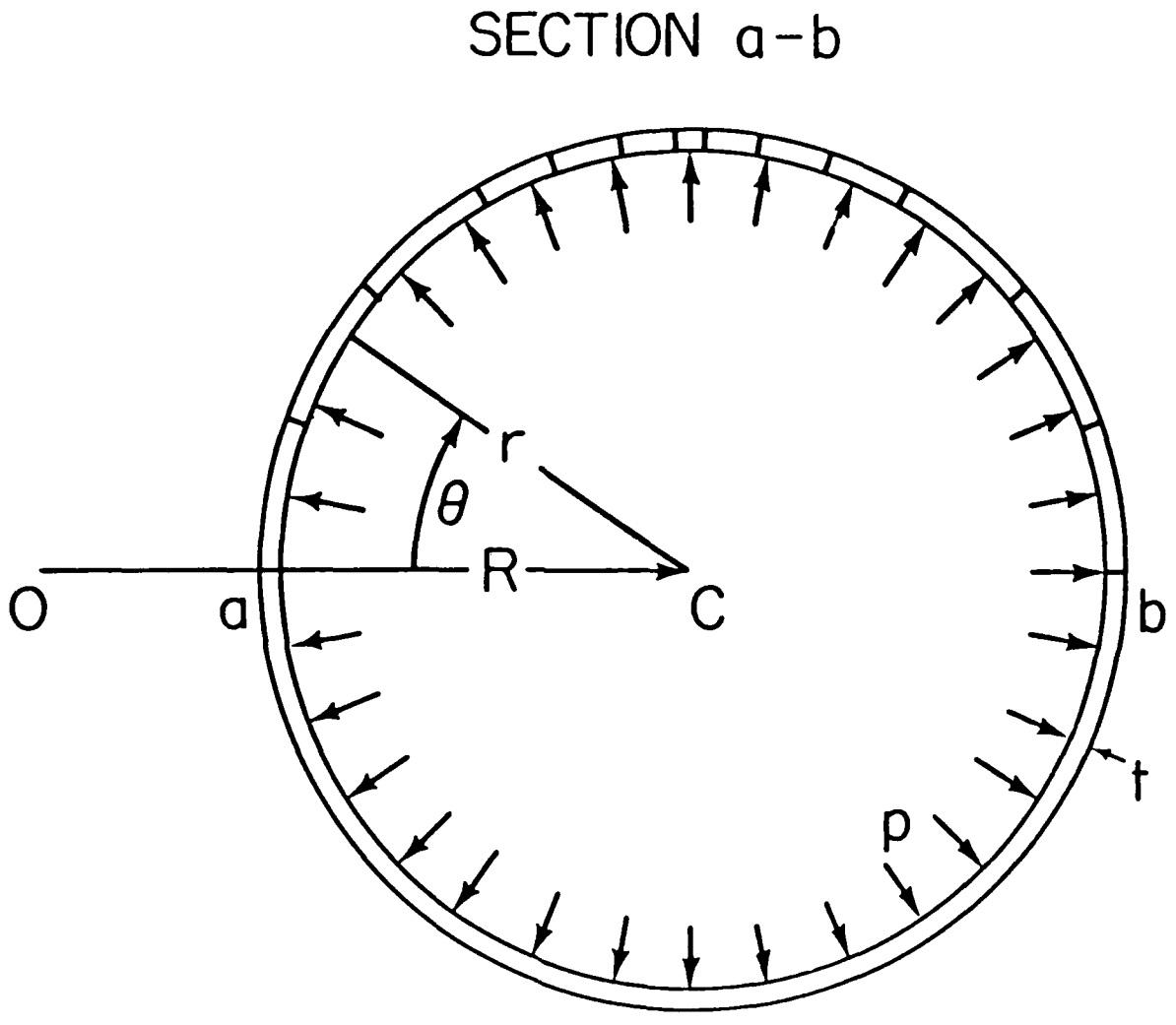

Figure 9(b) A toroidal shell under internal pressure p: section a-b

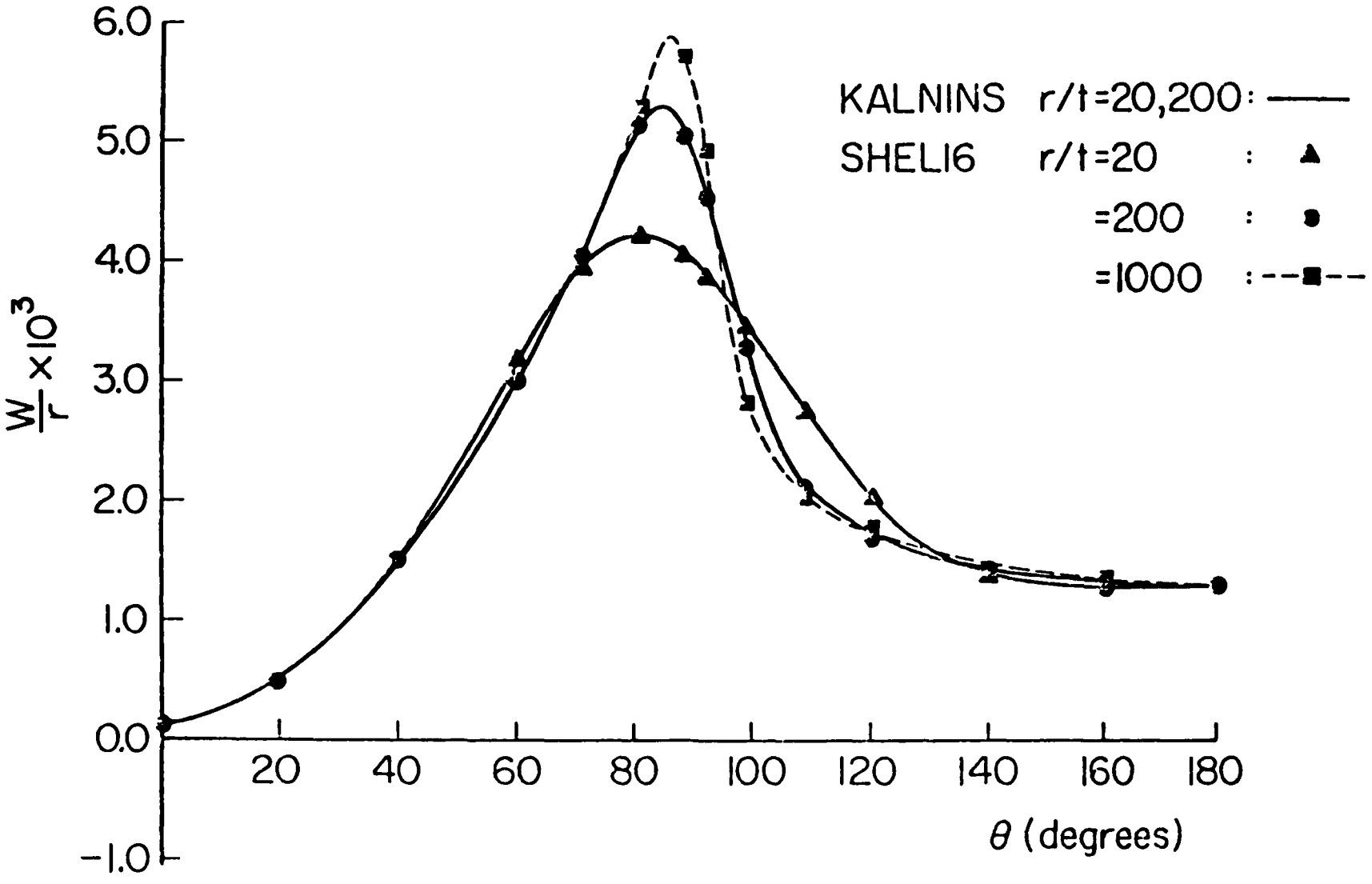

Figure 10 Normal deflection along meridional angle direction for the toroidal shell

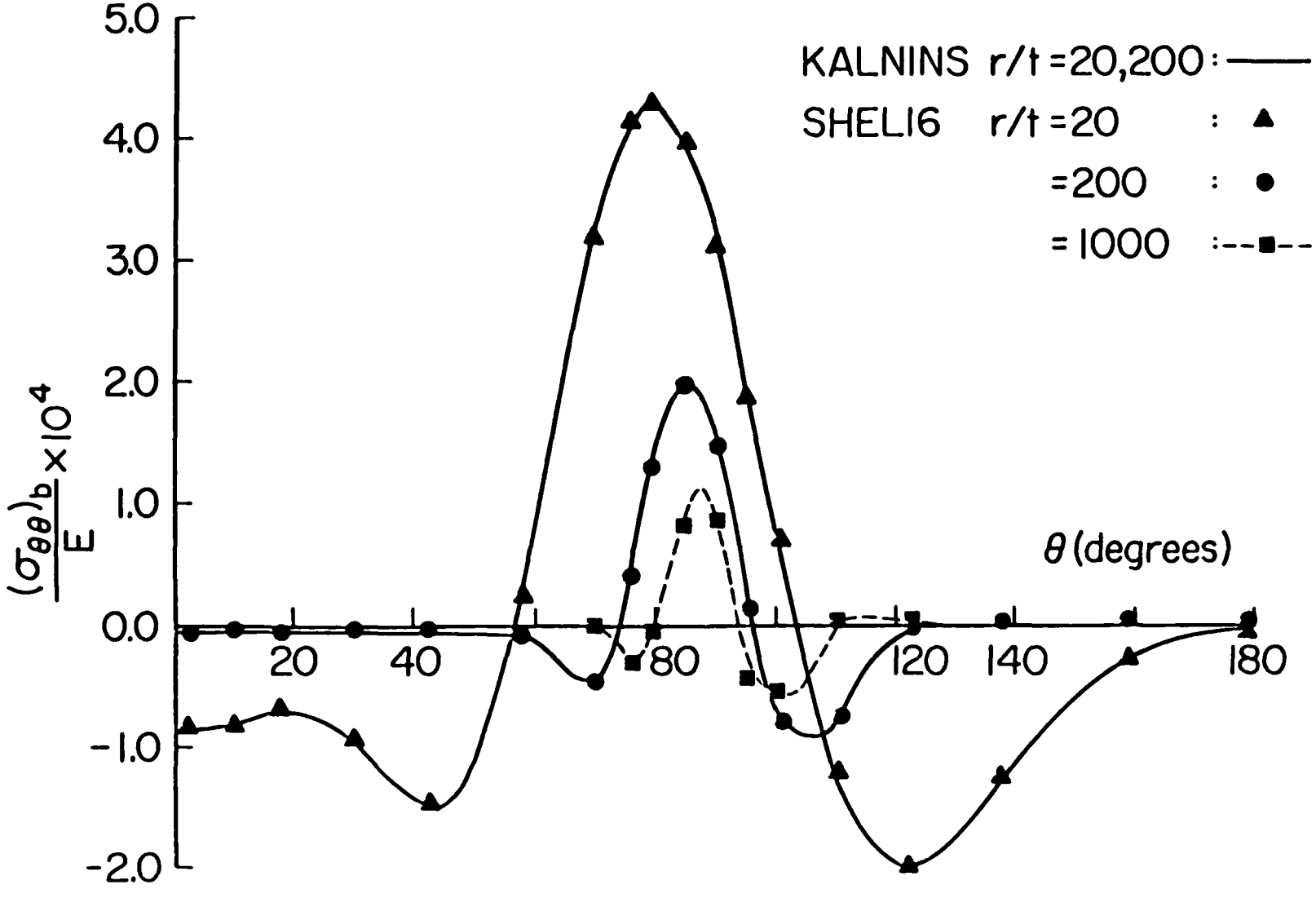

Figure 11 Bending stress along meridional angle direction for the toroidal shell

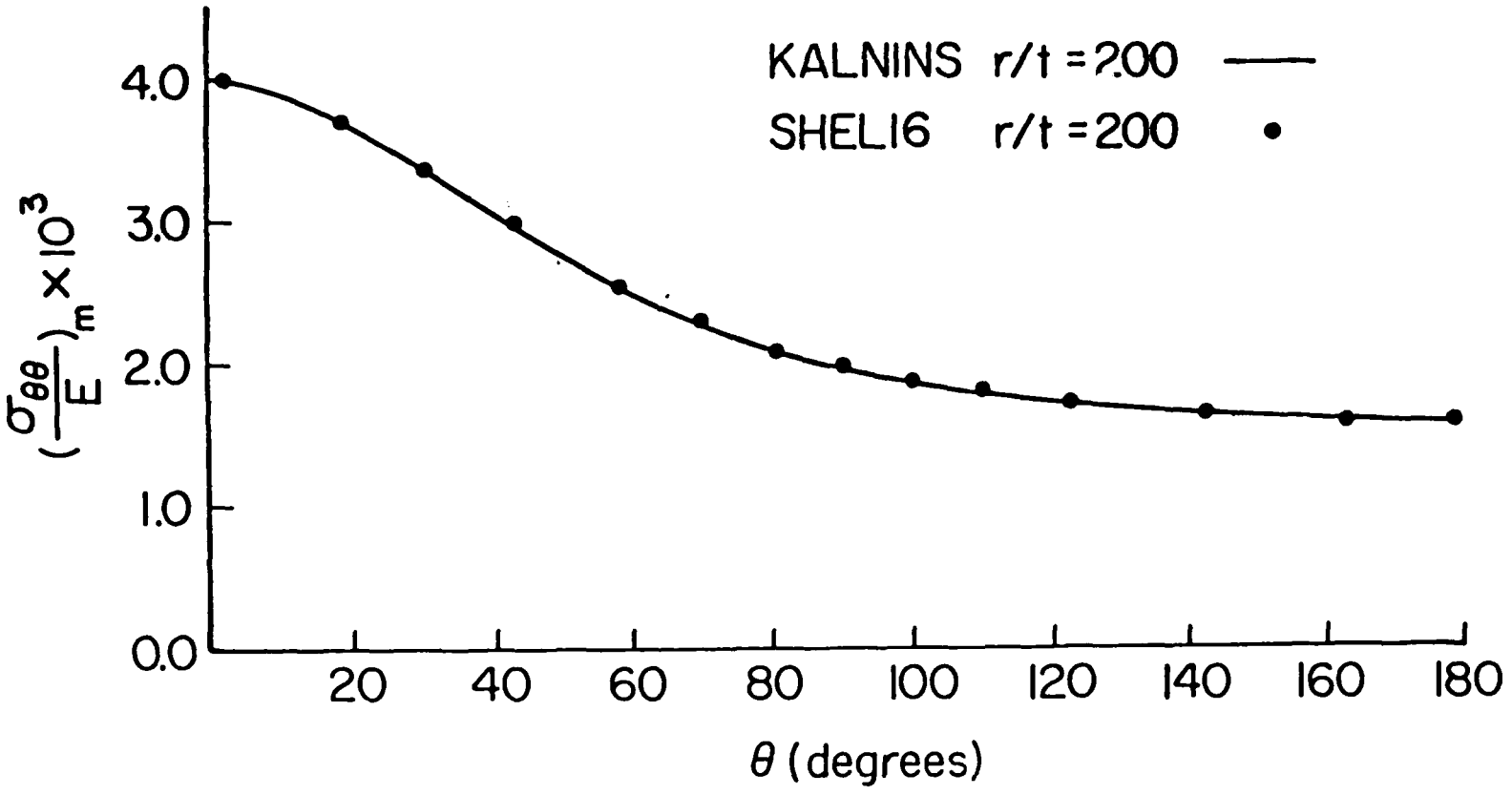

Figure 12 Membrane stress along meridional angle direction for the toroidal shell (r/t = 200)

END

9-87

DTIC